

# Simultaneous retrieval of aerosol and ocean properties from PACE HARP2 with uncertainty assessment using cascading neural network radiative transfer models

Meng Gao<sup>1,2</sup>, Bryan A. Franz<sup>1</sup>, Peng-Wang Zhai<sup>3</sup>, Kirk Knobelgesse<sup>1</sup>, Andrew Sayer<sup>1</sup>, Xiaoguang Xu<sup>3</sup>, Vanderlei Martins<sup>3</sup>, Brian Cairns<sup>4</sup>, Patricia Castellanos<sup>6</sup>, Guangliang Fu<sup>7</sup>, Neranga Hannadige<sup>3</sup>, Otto Hasekamp<sup>7</sup>, Yongxiang Hu<sup>5</sup>, Amir Ibrahim<sup>1</sup>, Frederick Patt<sup>1,8</sup>, Anin Puthukkudy<sup>3</sup>, and P. Jeremy Werdell<sup>1</sup>

<sup>1</sup>Ocean Ecology Laboratory, NASA Goddard Space Flight Center, Greenbelt, Maryland 20771, USA

<sup>2</sup>Science Systems and Applications, Inc., Greenbelt, MD, USA

<sup>3</sup>University of Maryland, Baltimore County, Baltimore, MD 21250, USA

<sup>4</sup>NASA Goddard Institute for Space Studies, New York, NY 10025, USA

<sup>5</sup>MS 475 NASA Langley Research Center, Hampton, VA 23681-2199, USA

<sup>6</sup>Global Modeling and Assimilation Office, NASA Goddard Space Flight Center, Greenbelt, Maryland 20771, USA

<sup>7</sup>Netherlands Institute for Space Research (SRON, NWO-I), Leiden, Netherlands

<sup>8</sup>Science Applications International Corp., Greenbelt, MD, USA

**Correspondence:** Meng Gao (meng.gao@nasa.gov)

**Abstract.** The UMBC Hyper-Angular Rainbow Polarimeter (HARP2) will be onboard NASA's Plankton, Aerosol, Cloud, ocean Ecosystem (PACE) mission, scheduled for launch in January 2024. In this study we systematically evaluate the retrievability and uncertainty of aerosol and ocean parameters from HARP2 multi-angle polarimeter (MAP) measurements. To reduce the computational demand of MAP-based retrievals and maximize data processing throughput, we developed improved neural

5 network (NN) forward models for space-borne HARP2 measurements over a coupled atmosphere and ocean system within the FastMAPOL retrieval algorithm. ATo this end, a cascading retrieval scheme is further implemented in FastMAPOL, which leverages a series of NN models of varying size, speed, and accuracy to optimize performance. Two sets of NN models are used for reflectance and polarization, respectively. A full day of global synthetic HARP2 data was generated and used to test various retrieval parameters including aerosol microphysical and optical properties, aerosol layer height, ocean surface wind

10 speed, and ocean chlorophyll-a concentration. To assess retrieval quality, pixel-wise retrieval uncertainties were derived from the Jacobians of the cost function error propagation and evaluated against the difference between the retrieval parameters and truth based on a Monte Carlo error propagation method. We found that the fine-mode aerosol properties can be retrieved well

15 from the HARP2 data, though the coarse-mode aerosol properties are more uncertain. Larger uncertainties are also associated with a reduced number of available viewing angles, which typically occurs near the scan edge of the HARP2 instrument. Results of the performance assessment demonstrate that the algorithm is a viable approach for operational application to HARP2 data after PACE launch.

## 1 Introduction

Satellite remote sensing has greatly enhanced our understanding of the Earth's environment, including the characterization of atmospheric aerosols and surface properties (Kaufman et al., 2002; Kokhanovsky et al., 2015; Kahn, 2015; Pörtner et al., In Press.). Multi-angle polarimetric (MAP) remote sensing, pioneered by the Polarization and Directionality of the Earth's Reflectances (POLDER) instrument on Advanced Earth Observing Satellites (ADEOS-I; 1996–1997 and ADEOS-II; 2002–2003) and the Polarization and Anisotropy of Reflectances for Atmospheric Sciences coupled with Observations from a Lidar (PARASOL; 2004–2013) mission (Tanré et al., 2011), has emerged as a promising approach for retrieving geophysical properties from Earth observations (Mishchenko and Travis, 1997; Hasekamp and Landgraf, 2007; Knobelispiesse et al., 2012; Lacagnina et al., 2017; Dubovik et al., 2019; Hasekamp et al., 2019b; Chen et al., 2022).

This trend is set to continue with the forthcoming launch of the National Aeronautics and Space Administration (NASA)'s Plankton, Aerosol, Cloud, ocean Ecosystem (PACE) mission in January 2024, featuring a hyperspectral scanning radiometer named the Ocean Color Instrument (OCI) (Meister et al., 2022) and two MAPs with high polarimetric accuracy: the University of Maryland, Baltimore County (UMBC) Hyper-Angular Rainbow Polarimeter (HARP2) (Martins et al., 2018; McBride et al., 2023) and the Netherlands Institute for Space Research (SRON) Spectro-Polarimeter for Planetary EXploration one (SPEXone) (Hasekamp et al., 2019a; Smit et al., 2019). The deployment of these instruments presents an unprecedented opportunity to enhance our understanding and representation of atmospheric and surface conditions (Remer et al., 2019a, b; Frouin et al., 2019), and bridge future MAP observations, such as the European Space Agency's (ESA) Multi-viewing Multi-channel Multi-polarisation Imager (3MI) on board the MetOp-SG satellites (Fougnie et al., 2018), and NASA's Multi-Angle Imager for Aerosols (MAIA) instrument (Diner et al., 2018).

Advanced simultaneous aerosol and surface property retrieval algorithms have been developed for MAP instruments (Chowdhary et al., 2005; Waquet et al., 2009; Hasekamp et al., 2011; Dubovik et al., 2011, 2014; Wang et al., 2014; Wu et al., 2015; Xu et al., 2016; Fu and Hasekamp, 2018; Li et al., 2018; Stamnes et al., 2018; Gao et al., 2018; Li et al., 2019; Hasekamp et al., 2019b; Chen et al., 2020; Fu et al., 2020; Puthukkudy et al., 2020; Gao et al., 2021a; Xu et al., 2021; Gao et al., 2023; Stamnes et al., 2023). Most of these retrieval algorithms developed for MAP observations are based on iterative optimization approaches that utilize vector radiative transfer (RT) forward models, capable to derive atmospheric and surface properties simultaneously. Constrained by the speed of forward model calculations, MAP retrieval algorithms are often computationally expensive, which limits their applicability for large-scale operational data production, and makes it difficult to conduct comprehensive uncertainty analyses. To address the data processing challenge related to MAP instruments, Di Noia et al. (2015) developed a neural network (NN) based retrieval algorithm that derives aerosol properties directly from groundSPEX (a ground-based version of the SPEX instrument) and RSP (Research Scanning Polarimeter, Cairns et al. (1999) [L](#)) measurements. These directly-inverted properties were then used as initial values in a subsequent iterative optimization.

To further improve the processing efficiency and flexibility, NN-based forward models are sometimes introduced to replace the radiative transfer calculation partially or fully in the retrieval algorithms. For example, Fan et al. (2019) [presented](#) [represented](#) the polarimetric reflectance for an open-ocean system using a NN and applied it to SPEXone data processing by

coupling with a linearized radiative transfer atmosphere model (Hasekamp and Landgraf, 2005). PACE HARP2 data poses a further challenge due to its large data volume, with a swath more than an order of magnitude wider than SPEXone's. Gao et al. (2021a) demonstrated that a NN-based ~~model~~-forward model can be trained to represent the vector radiative transfer calculation on a fully coupled atmosphere and ocean system. To process HARP2 data efficiently, the FastMAPOL algorithm was 55 developed, powered by such NN-based radiative transfer forward model and validated using AirHARP field campaign measurements (Gao et al., 2021a, b) and HARP2 synthetic data (Gao et al., 2021b, 2022). To enable data synergy from multiple PACE instruments, Stamnes et al. (2023) utilized NN-based forward models that combine spectral bands from both HARP2 and SPEXone in MAP retrievals. These recent developments build upon the successful application of NNs in non-polarimetric remote sensing (Diego and Loyola, 2004; Schroeder et al., 2007; Fan et al., 2017; Chen et al., 2018; Nanda et al., 2019; Shi 60 et al., 2020; Ukkonen, 2022; Stegmann et al., 2022; Ibrahim et al., 2022), and achieve the high radiometric and polarimetric accuracy of modern MAPs by using a larger number of hidden layers (e.g. three layers) and nodes (usually 200-1000).

Building from these studies, this work presents a refinement of the FastMAPOL retrieval algorithm suitable for global-scale PACE HARP2 data processing. The NN forward model is further optimized based on a realistic training data set, including expected orbital satellite geometries and employing highly accurate vector radiative transfer simulations. This allows us to test 65 the processing performance on global spaceborne data and illustrate the expected aerosol and ocean color retrieval performance of HARP2. We introduce a novel measurement-uncertainty-aware NN training via modification of its cost function resulting in a NN accuracy more consistent with the retrieval's cost function. Additionally, we explore the trade-off between NN speed and accuracy, training different sizes of NNs based on the new cost function, and further propose a cascading retrieval scheme that leverages a series of NN models of varying size, speed, and accuracy. Initial retrievals are conducted using faster, smaller, 70 but less accurate NN models, with subsequent retrievals performed using larger, slower, but more accurate NN models.

~~Based on this efficient retrieval algorithm which conduct simultaneous aerosol and ocean properties retrievals, a comprehensive set of aerosol properties are retrieved from simulated spaceborne HARP2 observations, including aerosol microphysical properties such as complex refractive index and size, thus extending the results obtained previously for AirHARP to realistic spaceborne measurements (Gao et al., 2021a). To improve understanding of aerosol vertical profile, we include aerosol layer 75 height (ALH) as one of the HARP2 retrieval products, as encouraged by the sensitivity studies conducted on RSP (Wu et al., 2016) and the HARP instrument (Xu et al., 2021). Additional aerosol optical properties, such as aerosol optical depth (AOD) and single scattering albedo (SSA), can be derived from aerosol microphysical properties also through neural networks (Gao et al., 2021a). These results provide a set of high quality aerosol products that will extend global polarimetric data records previously obtained from POLDER/PARASOL (Hasekamp et al., 2011; Dubovik et al., 2011, 2014; Li et al., 2019; Hasekamp et al., 2019b; Chen et al., 2020).~~

Meanwhile, the ocean properties can be derived from MAP retrieval results or measurements. Our previous work includes NN models to conduct atmospheric and bidirectional reflectance distribution function (BRDF) corrections and derive water leaving signals (Gao et al. 2021a, 2021b) and their uncertainties (Gao et al., 2022, 2023). Mukherjee et al. (2020) utilized a NN to predict the polarimetric reflectance associated with complex water optical properties. Aryal et al. (2022) used NNs to

85 derive instantaneous photosynthetically available radiation models within ocean bodies. Agaglate et al. (2023) applied a NN approach to estimate in-water optical properties from top of atmosphere MAP measurements for PACE.

To analyze the retrieval performance and uncertainties of these products, global over-ocean HARP2 radiative transfer simulations were generated using the most accurate NN forward model and the input parameters derived from NASA Modern-Era Retrospective analysis for Research and Applications, Version 2 (MERRA2) reanalysis data (Gelaro et al., 2017; Randles et al., 2017; Buch 90 . This effort is a part of the Day-in-the-Life (DITL) pre-launch data processing test organized by the PACE Science Data Segment (SDS). Through the global-scale data analysis based on the cascading-NN scheme in FastMAPOL, we examine the retrieval uncertainties for aerosol microphysical and optical properties in both fine and coarse mode aerosols modes, as well as ocean surface wind speed and ocean chlorophyll-a, with respect to the location, geometries, and distribution of geophysical properties. We have also included aerosol layer height (ALH) in the HARP2 retrieval products, as 95 encouraged by the sensitivity studies conducted on RSP (Wu et al., 2016) and the HARP instrument (Xu et al., 2021). The quantification of aerosol uncertainty can inform greatly enhance its applicability in radiative forcing (Jia et al., 2022), air quality (Wang and Christopher, 2003) and climate studies (Mishehenko et al., 2004). Consequently, this study offers a holistic discussion on the retrieval algorithm, the data products obtained, and the resultant data products with their associated uncertainties for HARP2 in anticipation of the upcoming PACE mission.

100 This study presents the advancements made to the HARP2 aerosol and ocean retrieval algorithm for operational data processing, including various improvements in the radiative transfer model with more realistic representation of space-borne measurements, effective NN training methodology, flexible NN architectures, and cascading retrieval scheme with comprehensive uncertainty assessment. The paper is organized in four sections, including a description of the retrieval algorithm and NN forward model (See Sect. 2), retrieval and uncertainty analysis on the global scale simulations (See Sect. 3), and conclusion with 105 discussions (See Sect. 4).

## 2 Improved FastMAPOL retrieval algorithm

This section provides an overview of the enhancements made to the FastMAPOL retrieval algorithm, with various improvements in the radiative transfer model, NN training methodologies, and retrieval schemes with cascading NN models.

### 2.1 Simultaneous aerosol and ocean retrieval algorithm

110 HARP2 measures Stokes parameters  $L_t$ ,  $Q_t$ , and  $U_t$  (where subscript t represent total measurement), at 60 viewing angles at the 660 nm band, and at 10 viewing angles at the 440, 550, and 870 nm bands (Puthukkudy et al., 2020, McBride et al 2023). The total spectral measured reflectance ( $\rho_t(\lambda)$ ) and DoLP (degree of linear polarization (DoLP or  $P_t(\lambda)$ )) are used in the retrieval inversion which are defined as

$$\rho_t = \frac{\pi r^2 L_t}{\mu_0 F_0}, \quad (1)$$

$$115 P_t = \frac{\sqrt{Q_t^2 + U_t^2}}{L_t}, \quad (2)$$

where  $F_0$  is the extraterrestrial solar irradiance,  $\mu_0$  is the cosine of the solar zenith angle,  $r$  is the Sun-Earth distance correction factor in astronomical units. Note that circular polarization (Stokes parameter  $V_t$ ) is not measured by HARP instruments and is often, but not always, negligible for atmospheric studies (Kawata, 1978; Gassó and Knobelspiesse, 2022).

To derive aerosol and ocean information, the retrieval algorithm minimizes the cost function  $\chi^2$  which quantifies the difference between the measurement and the forward model simulation (Rodgers, 2000):

$$\chi^2(\mathbf{x}) = \frac{1}{N} \sum_i \left( \frac{[\rho_t(i) - \rho_t^f(\mathbf{x}; i)]^2}{\sigma_\rho^2(i)} + \frac{[P_t(i) - P_t^f(\mathbf{x}; i)]^2}{\sigma_P^2(i)} \right), \quad (3)$$

where  $\rho_t$  and  $P_t$  are measurements and  $\rho_t^f$  and  $P_t^f$  are the corresponding quantities computed from the neural network forward model with the forward model. The state vector  $\mathbf{x}$  contains all retrieval parameters. The subscript  $i$  stands for the index of the measurements at different viewing angles and wavelengths; and  $N$  is the total number of measurements used in the retrieval.

The total uncertainties of the reflectance and DoLP used in the algorithm are denoted  $\sigma_\rho$  and  $\sigma_P$ ; both have contributions from measurement uncertainties ~~σ<sub>m</sub>~~ and forward model uncertainties  $\sigma_f$ . In this work, the estimated expected measurement uncertainty for HARP2 of 3% on reflectance and 0.005 on DoLP are used (McBride et al., 2023). Note that the above assumes independence of spectral or angular correlation between uncertainties; for a more complete treatment, Eq. 3 should be represented in a matrix form using the error covariance matrix (Rodgers, 2000; Gao et al., 2023). Statistical methods such as autocorrelation analysis have been used to estimate angular correlation strength from AirHARP field measurement and may be applied to future HARP2 data (Gao et al., 2023) but at present the correlation strength is not well-known so the above form (equivalent to a diagonal covariance matrix) is used. The retrieval is an iterative procedure to minimize the cost function using the subspace trust-region interior reflective optimization approach (Branch et al., 1999) by varying the state parameters  $\mathbf{x}$ . The In this work, the forward models are based on the NN discussed in the next sections and the Jacobian matrices, used to determine the direction to update the state parameter, are computed based on automatic differentiation (Baydin et al., 2018) as formulated for the NN forward model (Gao et al., 2021b) and implemented within the deep learning framework (Osawa et al., 2019).

## 2.2 Coupled atmosphere and ocean radiative transfer model

The training data for the NN forward model is generated with a PACE-tailored vector radiative transfer model using the successive orders of scattering method (Zhai et al., 2022) with numerical accuracy much better than that of the HARP instruments (Gao et al., 2021a). An improved pseudo spherical shell (IPSS) correction is considered to improve the fidelity for larger solar and viewing zenith angles (Zhai and Hu, 2022). Reflectance and DoLP are simulated at the PACE satellite altitude (676 km above Earth's surface); viewing and solar geometries are defined at the surface as shown in Fig. 1 based on the formulas derived in Zhai and Hu (2022).

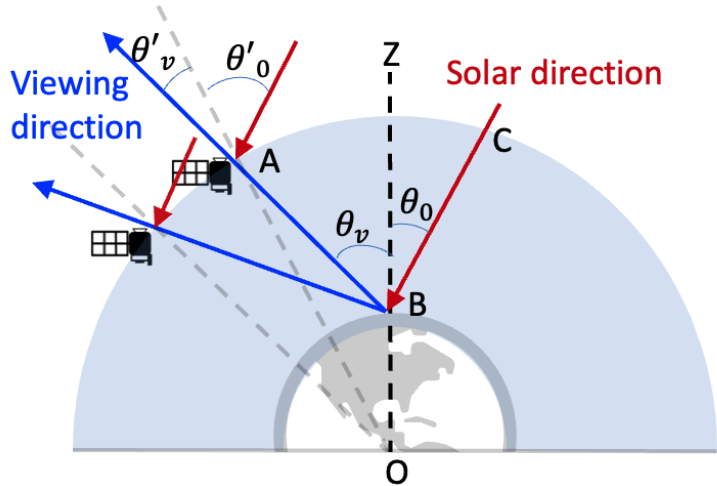


**Figure 1.** Spherical shell frame of the earth system. The radiative transfer simulations are conducted according to the geometry defined at the satellite with solar and viewing zenith angle  $\theta'_0$  and  $\theta'_v$ , which are converted to the geometry at the Earth's surface with solar and viewing zenith angle defined as  $\theta_0$  and  $\theta_v$ . Solar and viewing azimuthal angles also depend on the reference frame but [are](#) not shown in the figure.

145 The forward radiative transfer simulations are conducted assuming a coupled atmosphere and ocean system. The atmospheric molecule distributions follow the US standard atmospheric constituent profile (Anderson et al., 1986). Absorption by oxygen, water vapor, methane, and carbon dioxide, ozone and nitrogen dioxide are considered through line-by-line calculations and integrated based on the double-k method (Duan et al., 2005; Zhai et al., 2022). The ozone density and surface pressure are assumed in the range as defined in Table 1. Near the earth surface, an aerosol layer is considered with a vertical number density 150 distribution assumed as Gaussian function [Wu et al. \(2015\)](#)[\(Wu et al., 2015\)](#):

$$N(z) = \frac{N_t}{\sigma\sqrt{2\pi}} \exp\left(-\frac{(z - z_c)^2}{2\sigma^2}\right) \quad (4)$$

where  $N_t$  is the total aerosol column number density.  $z_c$  is defined as the aerosol layer height (ALH) in the range of 0.1 to 6 km above surface.  $\sigma$  is the standard deviation of the gaussian distribution which is fixed at 2 km. The aerosol size is represented by the volume density of a combination of five lognormally-distributed “submodes” similar to previous studies using the MAPOL 155 (Gao et al., 2018) and FastMAPOL algorithm (Gao et al., 2021a). The mean radius  $r_i$  and standard deviation  $\sigma_i$  are fixed with values of 0.1, 0.1732, 0.3, 1.0, 2.9  $\mu\text{m}$ , and 0.35, 0.35, 0.35, 0.5, 0.5, respectively following the work by Dubovik et al. (2011); Xu et al. (2016) and Fu et al. (2020). The first three submodes are used to represent the fine mode aerosol, while the last two submodes are the coarse mode. Fine and coarse modes are assumed to have an independent complex refractive index with no spectral variation within the HARP spectral range. Therefore, the aerosol model includes 10 parameters: five 160 volume densities (one for each submode); four independent parameters for the fine and coarse real and imaginary components of refractive indices; and one for ALH. Polarimetric single scattering properties are modeled from these [aerosol properties](#) using the Lorenz-Mie code on spherical particles developed by Mishchenko et al. (2002). Note that particle non-sphericity is

important for realistic simulation of mineral dust aerosols (Dubovik et al., 2006) and will be incorporated in the next version of NN forward model following the same approach presented in this study.

165 The optical model for the underlying water surface is summarized in Gao et al. (2019); briefly, it uses an open-ocean model including contributions from seawater, colored dissolved organic matter, and phytoplankton, the latter two of which are parameterized as a function of ~~chlorophyll-a concentration (Chla; mg/m<sup>3</sup>)~~<sup>chlorophyll-a concentration (Chl-a; mg m<sup>-3</sup>)</sup>. The sea water polarized scattering properties are derived from the measured normalized Mueller matrix (Voss and Fry, 1984; Kokhanovsky, 2003). The ocean surface roughness is modeled by the isotropic Cox-Munk model with a scalar wind speed (Cox 170 and Munk, 1954). Whitecaps are considered following the parameterization by wind speed (Koepke, 1984). While not done here, for future application to coastal waters where the open-ocean model is less valid, optimized NN models with sophisticated bio-optical models with seven (Gao et al., 2018) to three (Hannadige et al., 2023) parameters can be developed.

175 In summary, a total of 17 parameters are used as input of the NN forward model as indicated in Table 1. These include the 10 aerosol parameters, as well as wind speed, ozone column density, surface pressure and ~~Chla~~<sup>Chl-a</sup>, and three geometric parameters: the solar zenith angle, viewing zenith angle, and relative azimuth angle.

**Table 1.** Parameters used to represent the coupled atmosphere and ocean system in the radiative transfer simulation and NN Training.  $\theta_0$  and  $\theta_v$  are the solar and viewing zenith angles.  $\phi_v$  is the relative azimuth angle.  $V_i$  denotes the five volume densities. AOD range from 0.01 to 0.5 is considered and used to constrain  $V_i$ .  $m_r$  and  $m_i$  are the real and imaginary parts of the refractive index. Additional parameters include ozone column density ( $n_{O3}$ ), aerosol layer height ( $z_c$ ), surface pressure ( $P_s$ ), ocean surface wind speed ( $w_s$ ), and **Chlorophyll-a** concentration (**ChlaChl-a**). The minimum (min) and maximum (max) values determine the parameter ranges used to generate NN training data, which are also the constraints in the retrieval algorithm.

Parameters	Unit	Min	Max
$\theta_0$	Degree	0	85
$\theta_v$	Degree	0	85
$\phi_v$	Degree	0	180
$n_{O3}$	Dobson	150	450
$m_{r,f}$	(None)	1.3	1.7
$m_{r,c}$	(None)	1.3	1.7
$m_{i,f}$	(None)	0	0.03
$m_{i,c}$	(None)	0.	0.03
$V_1$	$\mu\text{m}^3\mu\text{m}^{-2}\mu\text{m}^3\mu\text{m}^{-2}$	0	0.14
$V_2$	$\mu\text{m}^3\mu\text{m}^{-2}\mu\text{m}^3\mu\text{m}^{-2}$	0	0.11
$V_3$	$\mu\text{m}^3\mu\text{m}^{-2}\mu\text{m}^3\mu\text{m}^{-2}$	0	0.07
$V_4$	$\mu\text{m}^3\mu\text{m}^{-2}\mu\text{m}^3\mu\text{m}^{-2}$	0	0.2
$V_5$	$\mu\text{m}^3\mu\text{m}^{-2}\mu\text{m}^3\mu\text{m}^{-2}$	0	0.62
$z_c$	$\text{km}$	0.1	6.0
$P_s$	mb	950	1050
$w_s$	$\text{m/s}$	0.5	15
<b>ChlaChl-a</b>	$\text{mg/m}^3\text{mg m}^{-3}$	0.01	10

### 2.3 NN training and performance analysis

The NN forward models (one set for reflectance and one set for **DOLPDoLP**) are trained following the procedures as summarized in Gao et al. (2021a) based on the radiative transfer simulations discussed in the previous section according to the parameter range as summarized in Table 1. This extends the previous work by including ALH and surface pressure as additional parameters, and the range of viewing geometries is also larger than the one used in the airborne measurement by taking advantage of the newly developed IPSS correction (Zhai and Hu, 2022) and the reference frame defined at the Earth's surface (Fig. 1). A total of 10,000 cases of radiative transfer simulations ~~with randomly-generated were generated with random~~ values of the input parameters (this set is augmented as described below). ~~Note that a~~ A uniform distribution of aerosol optical depth (AOD) ~~less than in the range between 0.01 and~~ 0.5 is ~~sampled, which is also used to compute randomly sampled and used~~

185 to specify volume densities following the sample strategy discussed in Gao et al. (2019) Gao et al. (2021a). In this study, we  
 introduce two additional steps in the NN training to boost the NN performance:

1. Measurement uncertainty-aware training

190 The NN forward models have been shown to achieve much higher accuracy than the HARP measurements using a LeakyReLU activation function and three hidden layers (Gao et al., 2021a). However, at low wind speed, the sunglint signal, i.e., the sunlight reflects from the ocean surface around the specular reflection direction, can be strongly peaked, and this can dominate the mean square error (MSE) cost function used by Gao et al. (2021a) for optimization at the expense of precision in other areas. To avoid this issue, the previous study removed simulations close to the direction of specular reflection from the training dataset, but the lack of data in sunglint also affected retrieval results due to the resulting reduced number of angles on wind speed and aerosol properties (Gao et al., 2021b). To enable sufficient 195 accuracy to predict the reflection inside and outside of sunglint, we introduce the training cost function that, analogously to the retrieval cost function, normalizes the fitting residuals by the measurement uncertainty:

$$\chi_{NN,\rho}^2 = \frac{1}{N} \sum_i \left( \frac{[\rho_t(i) - \rho_t^{NN}(\mathbf{x}; i)]^2}{\sigma_\rho^2(i)} \right) \quad (5)$$

$$\chi_{NN,P}^2 = \frac{1}{N} \sum_i \left( \frac{[P_t(i) - P_t^{NN}(\mathbf{x}; i)]^2}{\sigma_P^2(i)} \right) \quad (6)$$

200 where where  $\rho_t$  and  $P_t$  indicate training data, and  $\rho_t^{NN}$  and  $P_t^{NN}$  indicate the NN predictions.  $N$  in the denominator is the batch size in the training (taken as 1024 here). The same total uncertainty of  $\sigma_\rho = 0.03\rho_t$  and  $\sigma_P = 0.005$  as in Eq. 3 are used here. Therefore,  $\chi_{NN,\rho}^2$  represents the percentage error of the NN predictions, which can effectively incorporate the sunglint signals without directly impacting by its large magnitude. Since a constant value of  $\sigma_P$  is used,  $\chi_{NN,P}^2$  is equivalent to a scaled MSE cost function. Polarization signal is better constraint within 0 and 1 for all viewing geometries and therefore its training performance less affected by the sunglint. This new cost function is a convenient 205 and meaningful extension to the conventional MSE cost function applied on a set of normalized training data especially for reflectance (e.g. Aggarwal (2018); Fan et al. (2019); Gao et al. (2021a); Aryal et al. (2022); Stamnes et al. (2023)). We found the NN training hyperparameters (such as learning rate, batch size, etc) reported by (Gao et al., 2021a) generally Gao et al. (2021a) still work well for the new cost function. The resulting training process is aware of the measurement uncertainty and therefore optimizes in a way more relevant to the retrieval's operation.

210 2. Training data augmentation

Generating training data from forward radiative transfer simulations is usually computationally expensive, which limits the NN training performance. However, one RT simulation can be used to generate an arbitrary number of viewing angles and increase the effective training data size, which may improve NN accuracy. This concept is equivalent to data augmentation in machine learning (Shorten and Khoshgoftaar, 2019). Gao et al. (2021a) explored it by sampling 100 sets 215 of random viewing angles from every RT simulation. In this study, we provide a more systematic analysis of such data

augmentation by sampling random sets with 100, 400 and 1000 angles, corresponding to total data sizes of 1 million, 4 million, 10 million points respectively from the 10,000 RT simulations.

The NNs' training performance is summarized in Fig. 2 for the feed-forward NN architecture with 17 inputs and 4 outputs and various hidden layer sizes (from two layers each with 64 nodes and 128 nodes, to three layers each with 128, 256, or 512 nodes). To simplify the notation, we represent the hidden layer structure in a polynomial form, e.g.  $128^3$  in Fig. 2 represents 220 three hidden layers each with 128 nodes. **The cost functions are as in Eqs 5–6.** We use 70% of the simulated data for training (to minimize the training cost function) and the remaining 30% for validation (to monitor the training process). Fig. 2 shows that, with increasing NN hidden layer number and size, **both training cost functions** the cost functions for both training and 225 validation data decrease, while validation cost eventually becomes larger than training cost. That suggests overfitting for the case of 1 million samples and NN size  $128^3$ . Introducing more training data from 4 to 10 million and NN size until  $512^3$  further reduces the cost functions to convergence. More training data are generally able to reduce the difference between the training and validation cost function as compared in Fig. 2. Using 10 million total data, the reflectance NN performance stays stable with a small training cost function value of 0.01, which suggests the typical fitting residual between the NN and the simulation is about  $\sqrt{0.01} = 0.1$  times of the measurement uncertainty, i.e.,  $0.1 \times 3\% = 0.3\%$ .

230 For DoLP, the NN training is more difficult because the DoLP uncertainty for HARP2 is often much smaller (0.005) than the (3%) reflectance uncertainty. Fig. 2 shows that generally a larger NN size is needed for **DOLP** **DoLP** to achieve a similar cost function value to reflectance. Using 10 million data and  $512^3$  NN size, the cost function is about 0.04 which suggests the NN accuracy is  $\sqrt{0.04} = 0.2$  times of the measurement uncertainty, with a value of  $0.2 \times 0.005 = 0.001$ . Similar accuracy for NN reflectance requires a size of  $256^3$ . A NN cost function value of 1 would indicate NN accuracy comparable to the measurement 235 uncertainty, which would be achieved with a NN size of  $642$   $64^2$  for reflectance and  $4282$   $128^2$  for DoLP.

Therefore, for the best performance of applying NN in joint retrieval algorithms, we implemented a two-level cascade scheme in FastMAPOL in which two rounds of retrievals are processed. In the first round, the NN size of  $64^2$  for reflectance and NN size  $128^2$  for DoLP are used to efficiently find a rough solution. Then in the second (final) round the NN size  $256^3$  for reflectance and  $512^3$  for DoLP are used to further fine tune the state vector. Note that each retrieval include multiple iterations 240 with an order of 10, and involves the use of automatic differentiation to compute Jacobian matrix analytically (Gao et al., 2021b). Cascading more levels could further improve the performance, but we found two cascaded levels are sufficient for this study. **To** **By** **comparing** **the** **retrieval** **results** **with** **one** **and** **two** **cascading** **levels**, **we** **found** **the** **retrieval** **uncertainties** **are** **similar** **to** **each** **given** **the** **same** **high** **accuracy** **NN** **are** **used** **at** **the** **last** **level** **of** **retrievals**. **Therefore** **the** **cascading** **algorithm** **will** **increase** **retrieval** **speed** **without** **impact** **retrieval** **accuracy**. **To** **fully** **test** **the** **cascade** **system** **as** **discussed** **in** **the** **next** **section**, we used the 245 best accuracy NN with the largest size of  $512^3$  to generate a set of synthetic data simulations and performed retrieval with the cascade retrieval scheme in Section 3.

To further evaluate the NN uncertainty, we generated an additional independent 1000 sets of radiative transfer simulations with realistic HARP geometries as formulated in Gao et al. (2021b) and calculate MAE and RMSE comparing these simulations to the NN predictions. **Note** **We** **found** **that** MAE is more robust to the impacts of outliers, similar to the discussion on the retrieval uncertainties (Gao et al., 2022). Based on this analysis, discussed in Appendix 1, NN uncertainties are estimated to 250

be 0.5% for NN size of  $512^3$ , and 0.002 for  $\text{DOLP}$  using  $512^3$ , both similar to but slightly larger than estimation from the training cost function. This further confirms that the new training cost function, considering measurement uncertainty, provides an intuitive way to measure the NN optimization. Note that to ensure the high accuracy of the NN models, the RT simulations with a numerical accuracy much higher than the measurement and NN models are used to generate the training data as discussed in Gao et al. (2021a). For the application to real field measurements, the uncertainties including the NN models, RT simulations and the measurement uncertainties need to be considered.

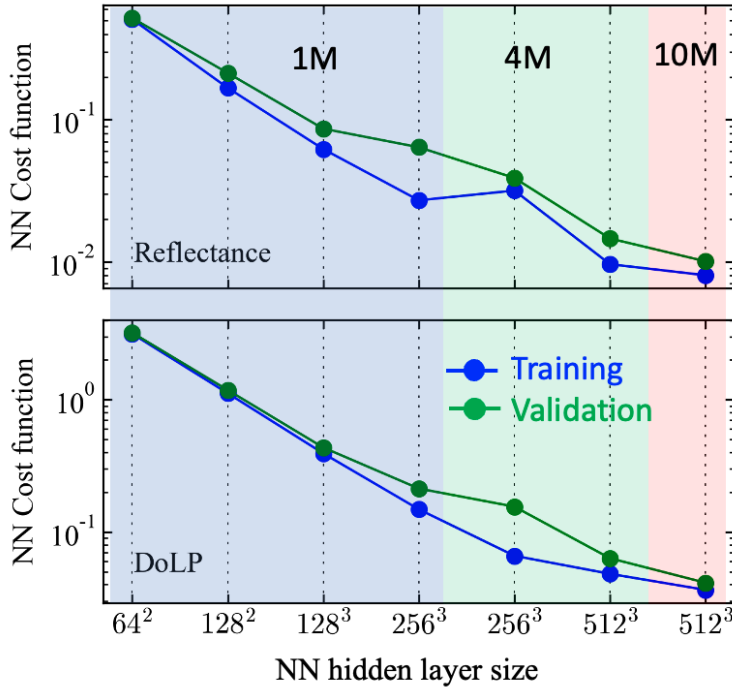


**Figure 2.** Training cost functions for reflectance (top) and  $\text{DOLP}$  as a function of NN size. The background color indicates the number of training data used: 1 million (blue), 4 million (green), or 10 million (red). The horizontal axis indicates the size of hidden layers, as described in the text, for example  $64^2$  indicates two hidden layers with 64 nodes at each layer. All the NN models shown here have 17 inputs and 4 outputs.

### 3 Retrieval analysis on synthetic global over-ocean HARP2 measurements

To evaluate the retrieval performance in terms of both speed and uncertainty in a realistic and representative way, we generated a day of synthetic over-ocean HARP2 measurement along PACE satellite orbits. Random errors based on estimated calibrated uncertainties are added to both the simulated reflectance and DoLP measurements. The retrieval uncertainties are evaluated through error propagation and then validated by comparing the truth and retrieval results based on the Monte Carlo approach

(Gao et al., 2022). The viewing and solar geometries are based on realistic satellite orbits. This analysis is useful to understand the retrieval capability of HARP2 data before PACE's launch.

### 3.1 Synthetic HARP2 L1C radiative transfer simulation

265 The Level 1C file format is used to represent multi-angle measurements where different viewing directions are co-registered on the common spatial location to produce multi-angle measurement for each pixel (Lang et al., 2019). For the PACE mission, a set of common spatial grids are defined within the L1C format for ~~its all~~ three instruments: OCI, SPEXone and HARP2. The grids are based on the swath-based Spacecraft Oblique Cylindrical Equal Area (SOCEA) projection (Snyder, 1987) and documented in the PACE L1C document (Plankton, Aerosol, Cloud, ocean Ecosystem (PACE) mission, 2020). The HARP2 data  
270 processing will be performed by the PACE Science Data Segment (SDS) following the launch and instrument commissioning. The prelaunch testing of the data processing has been organized around a Day-in-the-Life (DITL) that has been chosen to be March 21, ~~2022~~<sup>2022 (spring equinox)</sup>, to ensure good day light coverage over the majority of world's ocean. The simulated PACE orbit for the DITL has been used to generate the sensor and solar geometry for the instrument data simulations to support the data processing tests by the SDS. The HARP2 simulations and processing results described in the following sections are  
275 based on the DITL.

The PACE L1C files are segmented in 5 min granules for daytime portions of the orbit, yielding a total of 165 granules in 15 orbits as shown in Fig. 3. The equatorial crossing time is at 1:00 pm with the satellite ascending northward. The nadir swath width is 1633 km which grows to a maximum swath width of 2380 km around ~~40–40°~~ along track viewing zenith angle. The bin size is 5.2 km. The range of viewing zenith angle can vary from approximately  $-60^\circ$  to  $60^\circ$ , with data collected across a  
280 time span of 6 min during which the solar zenith angle can vary up to  $1.5^\circ$ . Exact per-view solar geometries were used when generating the synthetic HARP2 data, which is important to reduce impacts from the measurement geometries due to satellite motions (Hioki et al., 2021).

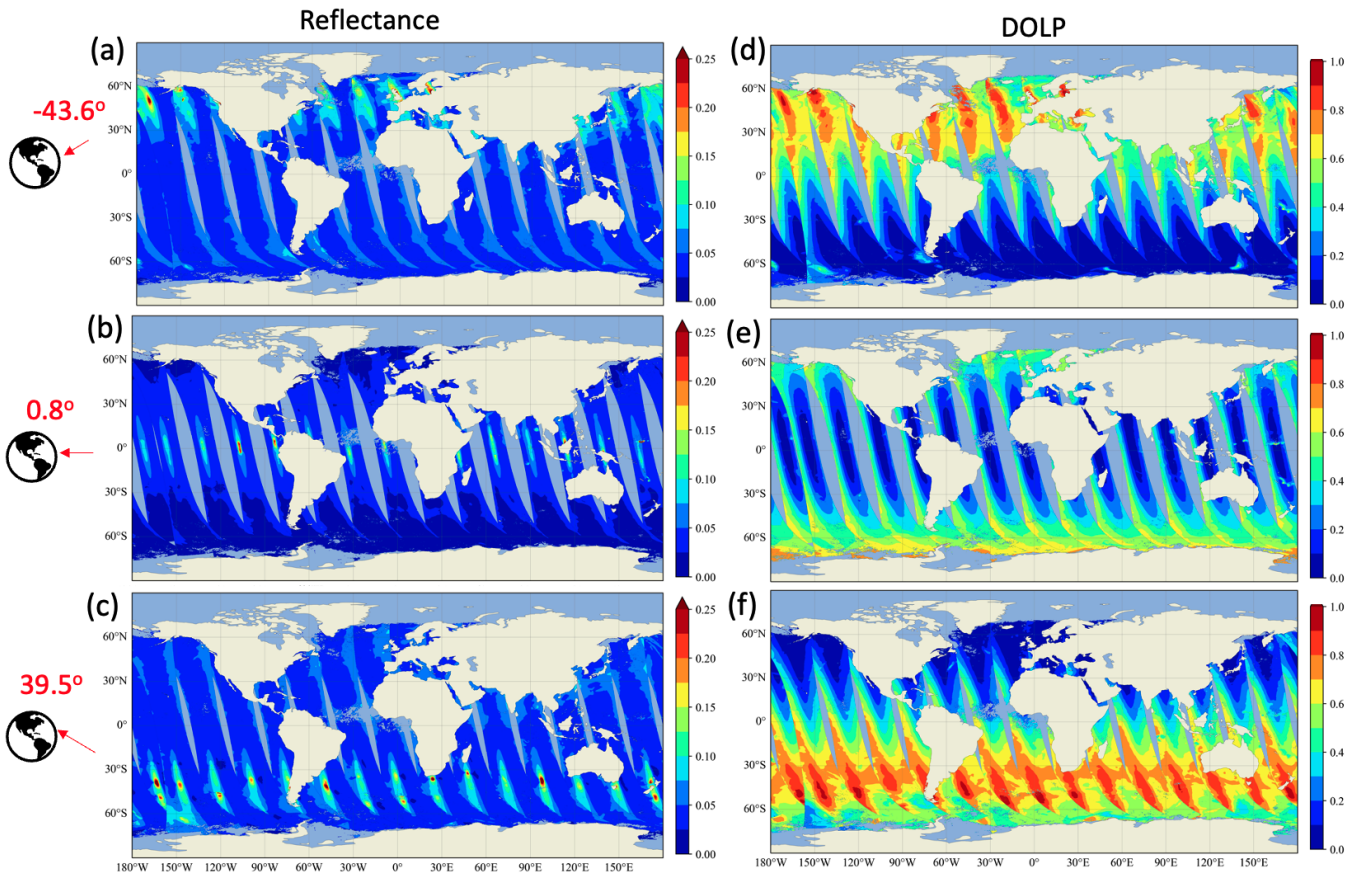


**Figure 3.** Global over-ocean simulation of HARP2 measurements at 550 nm for both reflectance (left) and DoLP (right) with a total of 15 orbits on the day of March 21, 2022. A total of 90 viewing angles at four HARP2 bands are generated with three viewing angles in the along-track direction shown in the plots.

In the simulation, the surface pressure, ozone column density, surface wind speed, and speciated aerosol mass concentration vertical profiles are sampled from the NASA GMAO MERRA2 data (Gelaro et al., 2017; Randles et al., 2017; Buchard et al., 285 2017) along the satellite orbit to best represent the natural global scale variability in the atmospheric state. Total column effective aerosol microphysical properties (column size and refractive index) were derived from the MERRA2 simulations of speciated aerosol mass concentration vertical profile by taking a volume weighted average over the size bins and species in the MERRA2 dataset. The aerosol size bins used in MERRA2 are different from the aerosol sub-modes used in the NN forward model. We have adjusted the volume density and refractive indices of the five aerosol sub-modes (see Table 1) to best match the 290 aerosol representation in MERRA2. Hygroscopic growth of aerosol size is considered based on the relative humidity profile in the MERRA2 data (Castellanos et al., 2019). The total AOD in MERRA2 data is used to derive the total volume density and ensure that the same AOD will be produced based on the column effective aerosol size, refractive index, and volume density. The monthly average Chla Chl-a derived from MODIS ocean color products are used as input to the radiative transfer

simulation. Note that there are some small data gaps, most visible in the tropical Atlantic Ocean, due to the gaps in this Chl-a product from heavy aerosol, cloud, or other data quality flags. However, as they are small the retrieval performance analysis should not be significantly impacted. A complete set of ancillary data files are generated and can be accessible from PACE data webpage as shown in the Data Availability section.

The NN forward model with the maximum accuracy ( $512^3$ ) is used to generate the simulated L1C data for a total of 10 million pixels each with 90 total viewing angles; examples for the HARP2 550 nm band with along-track viewing angles of  $-43.6^\circ$ ,  $0.8^\circ$  and  $39.5^\circ$  are shown in Fig. 3. The newly improved NN forward model can accurately represent the sunlilt region clearly recognizable from large reflectance magnitude at large viewing angles showing at northern (a) and southern hemisphere (c), as well as near equator (b) when looking near the nadir with a smaller reflectance magnitude. At larger viewing angles, prominent polarized signals are also shown in both the northern (d) and southern hemisphere (f). DoLP generally increases with the viewing angle, until approaching the maximum value of 1 at the Brewster angle around  $53^\circ$  at the air-water interface. The backscattering direction usually shows a minimum polarization magnitude, such as near the equator when looking near nadir (Fig. 3e).

Two cascaded NN forward models for reflectance and DoLP respectively are used to conduct retrievals in the FastMAPOL algorithm as discussed in Sect. 2. The histogram of the cost function values for the first and final retrievals are shown in Fig. 4. The first retrieval, whose NNs have comparable uncertainty to the measurement uncertainty, produces a most probable retrieval 310 cost function around 2.0. After using the more accurate NN with a much smaller uncertainty, the final retrieval cost functions are mostly close to 1.0. The average total time taken for a retrieval with this two-layer cascade is  $0.11 \pm 0.1$  seconds as shown in Fig. 4 (b), compared to 0.2 seconds for a retrieval using only the higher-accuracy NN (not shown), corresponding to roughly a 50% speedup.

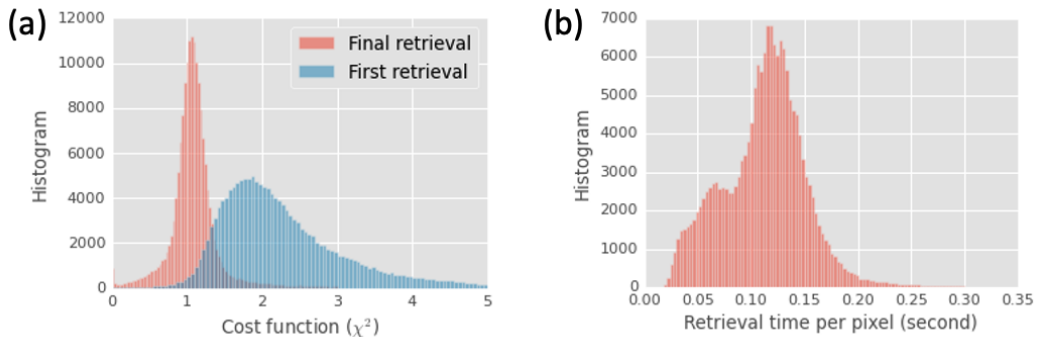


**Figure 4.** (a) Histogram of the cost function values ( $\chi^2$ ) for the first retrieval using smaller neural network (blue) and the final retrieval using the larger neural network (red) as summarized in See Sect. 2. A histogram of processing time for the two-stage process is shown in (b).

### 3.2 Retrieval results

315 Initially, we conducted a retrieval analysis on a subset of data by including all the parameters as shown in Table 1 except the three geometric variables. The retrieval uncertainties for the ozone density and surface pressure are large with a MAE of 53 DU and 24 mb and RMSE value of 69 DU and 32 mb, respectively. As a result, instead of retrieving these two parameters, we choose to use the value directly from MERRA2 and retrieve only aerosol and ocean properties (which also results in slightly increased accuracy) when applying FastMAPOL to the L1C simulated data. As well as the directly retrieved quantities (Table 320 1), the aerosol optical depth (AOD) and single scattering albedo (SSA) for both the fine and coarse modes, were computed from retrieved aerosol volume densities and refractive indices using corresponding NNs trained similarly to the reflectance and DoLP but with a much smaller size of two hidden layer each with 64 nodes (Gao et al., 2021a). Total AOD is obtained as the summation of the fine and coarse mode AODs. Effective radius and variance are also calculated from the components' sizes and retrieved volumes.

325 Fig. 5 shows the global map of the retrieved AOD and ALH as well as the corresponding truth values and the retrieval uncertainties based on error propagation. The retrieval value and truth values are very similar to each other as shown in Fig. 5 (a) and (b) for AOD. Larger uncertainties are mostly associated with the edge of the orbit where fewer than five viewing angles per band (or total 20-30 angles) are available (see also analysis in Hasekamp and Landgraf (2007); Wu et al. (2015); Xu et al. 330 (2017); Gao et al. (2021b)). For real PACE data, the adaptive data screening method will be used to automatically remove the angles impacted by cirrus cloud and anomalies, and therefore, the uncertainties will depend on the number of available angles associated with the location and size of those clouds (Gao et al., 2021b). Fig. 5e and 5d show that the aerosol layer height (ALH) error has a stronger dependency on the AOD with performance generally better (and uncertainties smaller) where AOD is larger.

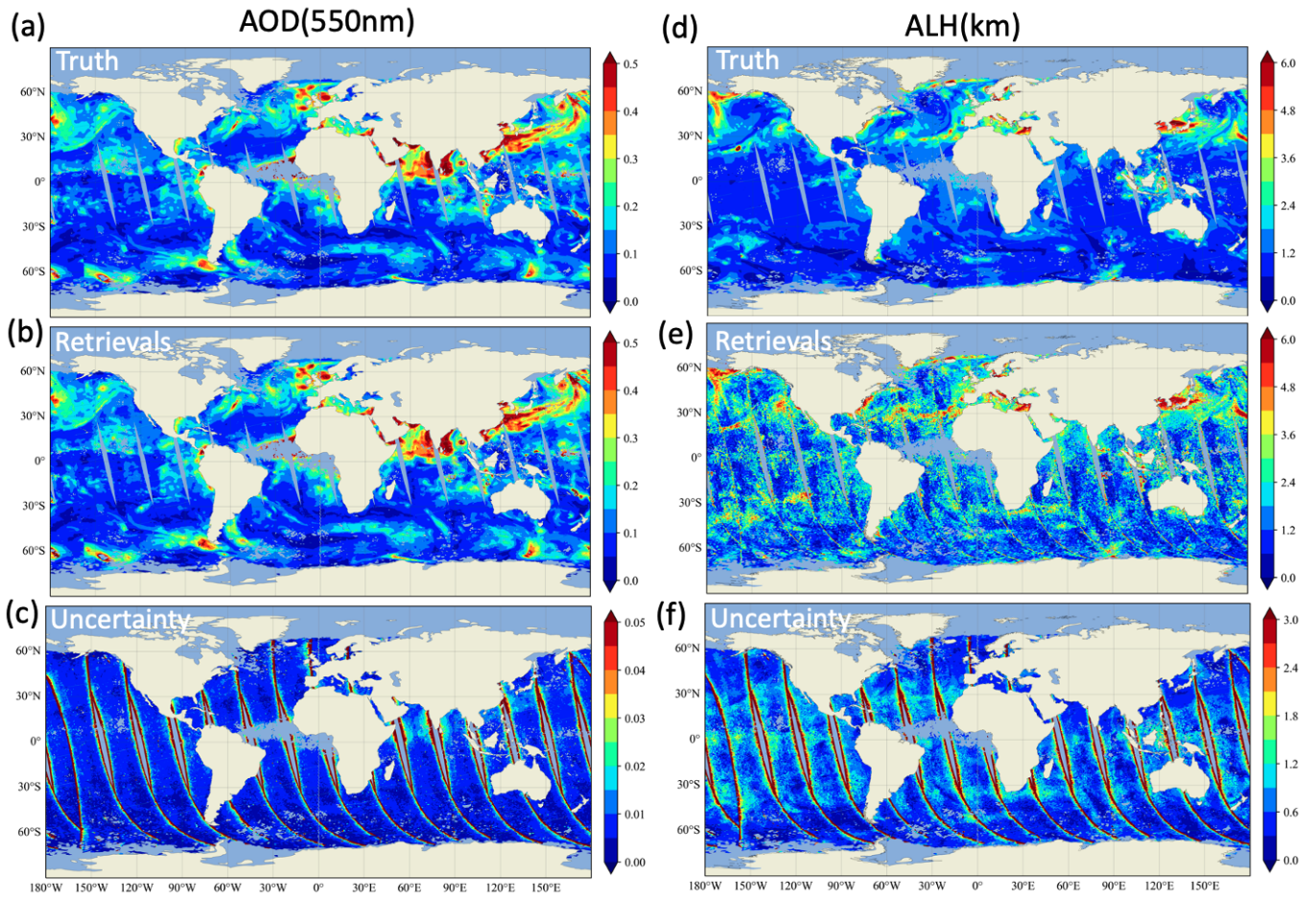


**Figure 5.** The retrieval results, truth, and uncertainties for AOD at 550 nm (a, b, c) and ALH (d, e, f).

335 Data density showing the correlation and difference between retrieval and truth are shown for AOD, ALH, fine mode volume  
 fraction (fvf), wind speed, and Chl-a in Fig. 6. The retrievals perform well with the RMSE for AOD, ALH, fvf, wind  
 speed and  $\log_{10}(\text{Chl-a})$  of 0.011, 0.9 km, 0.06,  $1.4 \text{ ms}^{-1}$  and 0.19 respectively. Similar to Fig. 6, Fig. 7 shows the  
 comparison between the retrieval results with truth for the fine mode AOD at 550nm, real part refractive index, single scattering  
 albedo, effective radius and variance. The difference between retrieval and truth seems to strongly depend on the fine mode  
 aerosol loading as shown in the second row of Fig. 7. However, the retrieval becomes more challenging for the coarse mode as  
 340 shown in Fig. 8, due to the much lower coarse AOD in general.

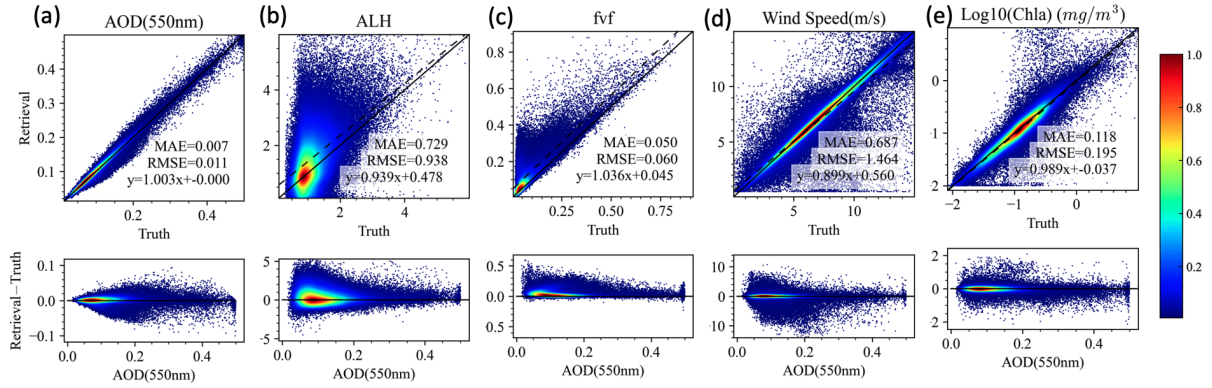


**Figure 6.** The comparisons of the retrieved and truth values for total AOD (550 nm), ALH, fine mode volume fraction (fvf) wind speed, and ChlaChl-a. The top row shows heat maps (including MAE and RMSE) while the bottom row shows the error of the corresponding upper panel parameters as a function of the total AOD at 550 nm. The color indicate the data density estimated by a kernel density method (Silverman, 1986).

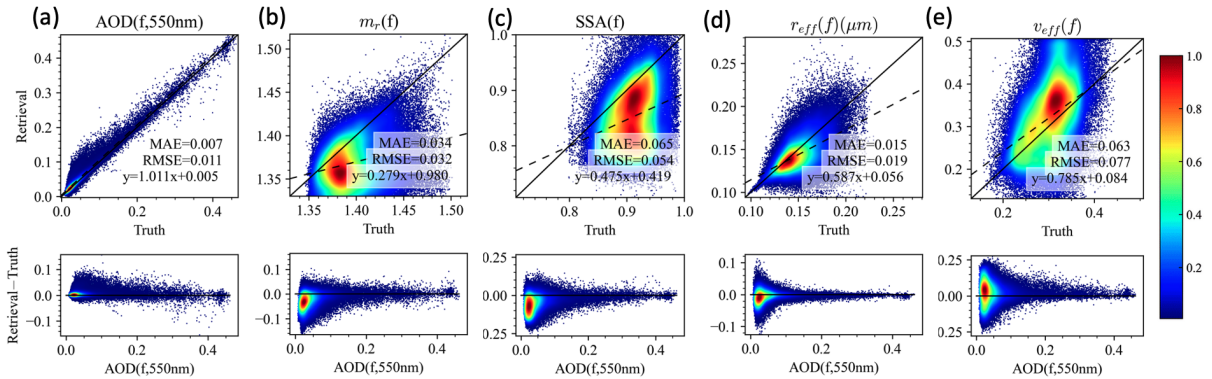


**Figure 7.** As Fig. 6, except for fine mode AOD, refractive index ( $m_r$ ), SSA, effective radius ( $r_{eff}$ ) and variance( $v_{eff}$ ) and bottom row as a function of fine mode AOD.

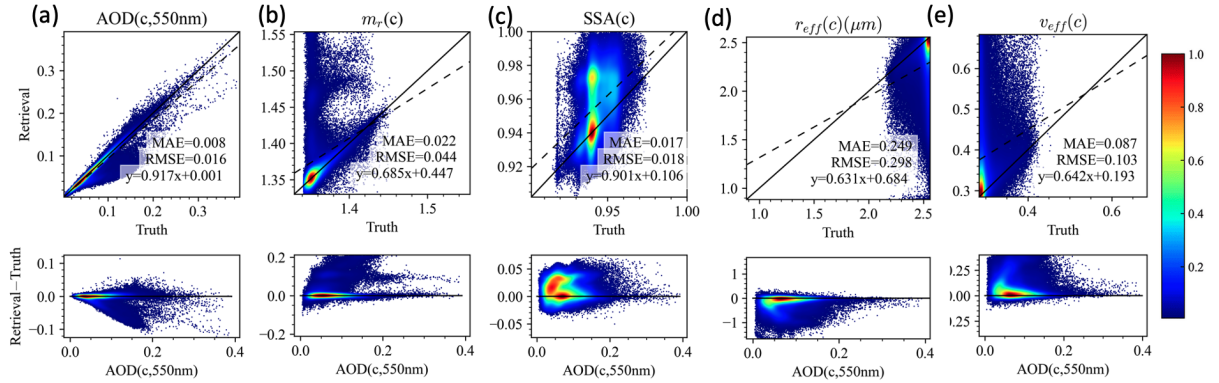


**Figure 8.** As Fig. 7, except for coarse mode properties instead of fine mode.

### 3.2.1 Uncertainty analysis

To understand the quality of the retrieval products, “theoretical retrieval uncertainties” are evaluated from error propagation method which maps the measurement uncertainties to the retrieval domain based on the Jacobian ~~of the converged retrieval cost function with converged retrieval parameters~~ (Rodgers, 2000) and accelerated using NN automatic differentiation (Gao 345 et al., 2021b). This uncertainty can be evaluated at every pixel and therefore provide a flexible metric to evaluate retrieval quality. Examples of AOD and ALH uncertainties are shown in Fig. 6 (c) and (f). However, the real retrieval quality also depends on how well the retrieval converges, which can be eventually evaluated based on the difference between the retrieval 350 results and the truth as shown in Figs 6-8. To verify ~~that~~ the theoretical retrieval uncertainty represents actual retrieval results, we employ the Monte Carlo Error propagation (MCEP) method, which generates random samples of errors based on the theoretical uncertainties. ~~The Then, the~~ histogram of the random errors for a large volume of dataset can be compared with the distribution of the real error (difference between retrieval and truth) so that we can assess the difference and similarity of error distribution derived from the two methods (Gao et al., 2022).

We further group all the pixels according to their AOD values in steps of 0.01. ~~Based~~ ~~on~~ the retrieval results shown in Figs 6-8. Mean absolute error (MAE) are used to evaluate both the average theoretical and real uncertainties with results 355 summarized in Fig. 9. ~~As AOD increases from 0.01 to 0.45, the uncertainty of AOD increases from 0.002-0.004 to 0.015, corresponding to a relative reduction of uncertainty from 20%-40% to 5%. The results agree with the analysis on AirHARP and HARP2 measurements of Gao et al. (2021a, b). Points with AOD>0.45 are excluded because there are a small number of pixels in this range so that a few outliers could affect the statistics significantly.~~ Fig. 9(a1) shows that both the theoretical (red lines) and the true (blue lines) absolute uncertainties of AOD increase from 0.002-0.004 to 0.015 as AOD increases 360 from 0.01 to 0.45, which also corresponds to the reduction of relative uncertainty from 20%-40% to 5%. The results agree with the analysis on ~~AirHARP and synthetic~~ HARP2 measurement with a uniform distribution of AOD (Gao et al., 2021a, b). ~~(Gao et al., 2021b, 2022). Points with AOD>0.45 are excluded because there are a small number of pixels in this range so that~~

a few outliers could affect the statistics significantly. The high quality AOD may be useful for climate studies which usually require a goal uncertainty less than 0.02 (Mishchenko et al., 2004; Kahn, 2015; GCO, 2022).

365 Uncertainties of ALH decrease from 1 km to 0.5 km within the range of AOD for both theoretical and real uncertainty. The retrieval uncertainty is larger than the results from the RSP instrument using a spectral range of 410-1590 nm, where the MAE between the true the retrieval values is less than 250 m ([Wu et al., 2016](#)), ([Wu et al., 2016](#)), probably as HARP2's shortest wavelength is 440 nm and it has a larger polarimetric uncertainty of 0.005 comparing with RSP (0.002). However, the ALH can be still useful for radiative forcing studies (e.g., Jia et al. (2022)) and air quality investigations (e.g., Wang and Christopher 370 (2003)).

Due the wide angular range and the inclusion of sunglint signals in the NN forward model, the real wind speed accuracy are found much higher ( $1 \text{ m s}^{-1}$ ) comparing to previous studies of  $2\text{-}3 \text{ m s}^{-1}$ , although the smaller theoretical uncertainties  $\text{s}^{-1}$  ([Gao et al., 2022](#)). The theoretical uncertainty has a smaller value around  $0.5 \text{ m s}^{-1}$ , which suggest further room for retrieval improvement. The Chla-Chl-a uncertainties are evaluated as the MAE of the  $\log_{10}(\text{Chla-Chl-a})$  uncertainty as recommended by

375 Seegers et al (2018):

$$\text{MAE}(\log) = 10^Y \text{ where } Y = \frac{1}{N} \sum_{i=1}^N |\log_{10}(R_i) - \log_{10}(T_i)| \quad (7)$$

where  $R_i$  and  $T_i$  denote the retrieval and truth values. This “multiplicative error” is a relative, dimensionless metric and takes values of 1 or more, where 1 indicates no error, 1.5 indicates a 50% error, and so on. Fig. 9 e1 shows that Chla-Chl-a can be retrieved accurately with a ratio mostly less than 2.0, which suggests potential of the MAP data for the evaluation of ocean 380 properties. However, this would become challenging when the ocean water optical properties are more complex (Gao et al., 2019). Larger differences between the theoretical and real uncertainties are found mostly at AOD  $>0.2$ , as the ocean signal becomes increasingly obscured by the aerosols.

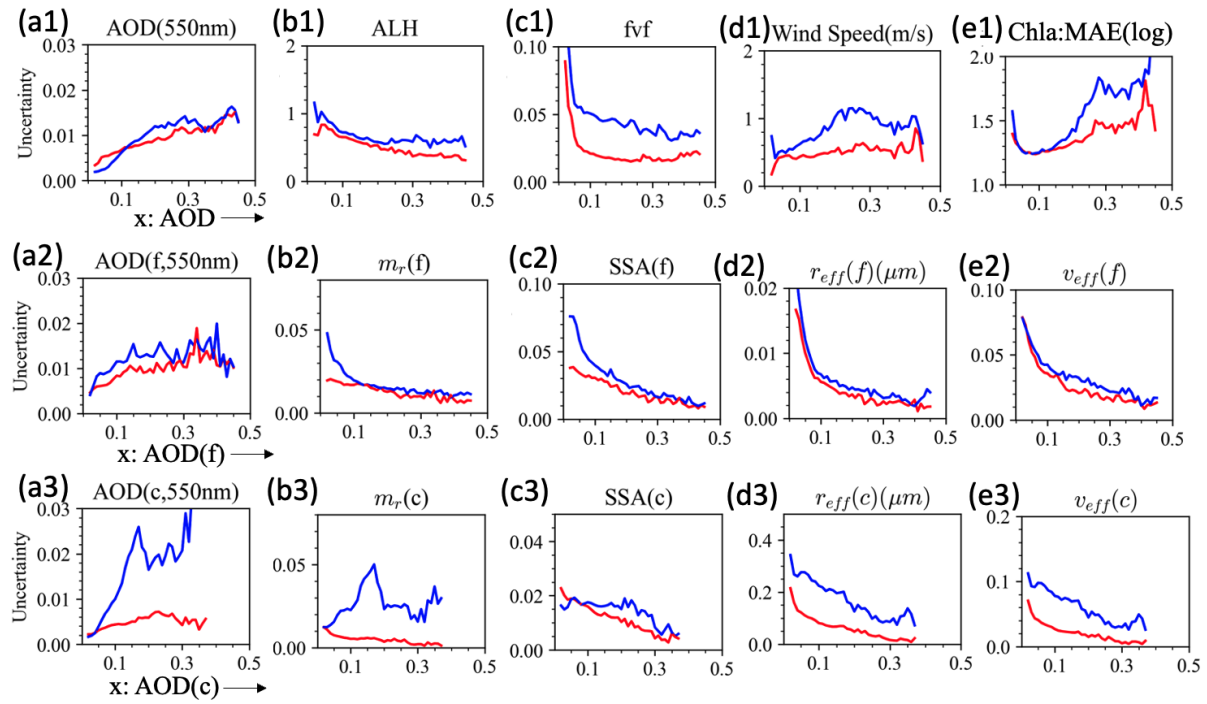


**Figure 9.** Comparison of theoretical (red) and real retrieval uncertainties (blue) as a function of AOD for AOD, SSA, real part of refractive index ( $m_r$ ), effective radius ( $r_{eff}$ ) and variance ( $v_{eff}$ ), wind speed, and Chla:MAE(log). AOD, fine mode AOD, and coarse mode AOD values are used at the x-axis from 0.01 to 0.45 with a step of 0.01.

For the fine mode, theoretical and real uncertainties are compared in Fig. 9 (a2-e2). Fine mode AOD seems to perform similarly to total AOD. The theoretical uncertainties agree with the real uncertainties when fine mode AOD is larger than 0.1 but underestimate real uncertainties when AOD is lower. This may indicate smaller sensitivity and larger instability due to the impacts of local minima in cost function. However, the theoretical uncertainty seems to capture the real uncertainty well for effective radius and variance across the range of fine mode AOD.

For the coarse mode, as the range of the coarse mode imaginary refractive index in MERRA2 is limited (mostly  $< 0.001$ , probably due to the dominance of sea salt or other coarse soluble aerosols), we limited the retrieval of this parameter to a similar range. The large spread of retrieved SSA in Fig. 8 (c) suggests the lack of sensitivity on the retrieval of coarse mode imaginary refractive index. The uncertainties are captured well by the theoretical uncertainties by Fig. 9(c3). After launch, sensitivity studies will be required to better prescribe the coarse mode imaginary refractive index. From the current synthetic data analysis, the real uncertainties are much larger than the theoretical uncertainties for coarse mode properties. Low sensitivity is expected due to the low aerosol loading and lack of longer-wavelength shortwave infrared (SWIR) bands and therefore the challenges to converge to the global minimum of the cost function. The real uncertainties on coarse AOD are much larger than the fine mode uncertainties with a value up to 0.03, although the theoretical uncertainty for coarse mode AOD is smaller (0.002-0.005) than the fine mode AOD uncertainty (0.005-0.015), possibly due to the stronger constraint on the coarse mode

absorption. For PACE data, a future synergy with the SWIR bands from OCI may be used to improve the coarse mode retrieval quality (Hasekamp et al 2019). However, the impact of the coarse mode aerosols in the application of atmospheric correction  
400 may be less severe due to its small overall value and weak spectral variation.

#### 4 Discussion and conclusions

In this study we ~~illustrate improvements to the radiative transfer behind and computational practicality of the FastMAPOL retrieval algorithm tailored to the HARP2 sensor. We also systematically investigate the retrievability of aerosol and ocean parameters and their uncertainty. The retrieval algorithm was greatly improved by incorporating high performance NN forward models trained for the~~ illustrated the advancements made to the FastMAPOL retrieval algorithm, including various improvements in the radiative transfer model, NN training methodology, NN architecture, and retrieval scheme:

- ~~Radiative transfer model: We improved the radiative transfer model which are used to generate the training data for space-borne HARP2 measurements. The computational challenges in processing MAP data are further reduced by applying a cascaded approach in FastMAPOL in a two-step retrieval with a processing time of 0.11 s using a single AMD EPYC processor. The speed to process a single PACE L1C 5 min granules with roughly  $400 \times 400$  pixels can be finished within 5 hours in a single CPU core. This illustrates that global-scale MAP data processing is feasible. measurement by including spherical shell correction, realistic solar and viewing geometries, additional input parameters such as surface pressure and aerosol layer height.~~
- ~~A full day of the global synthetic HARP2 data were generated based on the newly improved neural network forward model. The synthetic dataset was fed to FastMAPOL to analyze the retrieval uncertainties for the~~
- ~~Training methodology: The NN models are trained by incorporating the measurement uncertainty model in the training cost function which better represent sunglint signals and help improve the NN relevance to the retrieval's operation.~~
- ~~NN architecture: Flexible NN models with various number of hidden layers and number of nodes are investigated, which achieve different speeds and accuracies.~~
- ~~Retrieval scheme: Two levels of NN models with increasing sizes and accuracies are used in a cascading retrieval scheme to achieve high retrieval efficiency and performance.~~

With the improved NN models and retrieval schemes, we also systematically investigate the retrievability of aerosol and ocean parameters and their uncertainty. The retrieval uncertainties are analyzed based on the FastMAPOL retrievals on the synthetic datasets, including the aerosol optical properties such as AOD and SSA, and microphysical properties including aerosol size, refractive index, and height with more realistic statistics of the parameter values and viewing and solar geometries. For example, the overall uncertainties for AOD and wind speed are 0.01 and  $1.4 \text{ ms}^{-1}$ . The retrieval uncertainties at the pixel level are shown to depend on the number of available viewing angles and the aerosol loading. Fine mode aerosol properties, such as aerosol refractive index, generally show smaller retrieval uncertainties, and better agreement between error propagation

uncertainties and real uncertainties from simulated retrievals. Coarse mode aerosol retrieval uncertainties are larger and not  
430 fully captured by error propagations. ~~Furthermore, we~~ ~~We~~ also demonstrated, HARP2 measurements ~~contain sensitivity can be~~  
~~used~~ to derive aerosol layer height with an uncertainty of 0.5 to ~~1km~~ ~~1.0 km~~ depending on the aerosol loading.

Based on retrieval results, water-leaving signals can be derived. Regarding the retrieval speed, in a previous version of the  
FastMAPOL algorithm we employed NN forward models with analytical Jacobian evaluation based on automatic differentiation,  
which had expedited the processing of the AirHARP data from one hour per pixel using on-the-fly radiative transfer forward  
435 model simulations to around 0.3 second per pixel (Gao et al., 2021a, b). In this study, the processing speed of the HARP2  
synthetic data is further improved to about 0.2 second per pixel by optimizing the numerical code. It is further reduced to 0.1 s  
using a single CPU core by applying a cascaded approach in FastMAPOL. With the newest development the speed to process  
a single PACE L1C 5 min granules with an order of 400 x 400 pixels can be finished within 5 hours in a single CPU core.  
As already demonstrated in our system, the whole day of synthetic data were processed within 5 hours by utilizing distributed  
440 computing and running all granules parallelly. This illustrates that global-scale MAP data processing is feasible.

Furthermore, additional ocean properties can be derived from the MAP measurements and retrieval results. For example, NN  
models based on the ~~retrieved~~ aerosol and ocean parameters have been used to obtain water-leaving signals through the atmospheric  
and BRDF corrections on ~~all~~ HARP angles, both represented by NN (Gao et al., 2021a). The real or synthetic AirHARP  
and HARP2 measurements (Gao et al., 2021a, 2022). Similarly, the retrieved aerosol properties ~~may~~ can be used to assist the  
445 hyperspectral atmospheric correction on PACE OCI (Gao et al., 2019; Hannadige et al., 2021). Furthermore, multi-angle data  
screening can be applied to mitigate impacts from cirrus cloud and other anomalies (Gao et al., 2021b), and derive multi-angle  
water-leaving signals. The results will be provided in a future study, as demonstrated using SPEX data as a PACE OCI proxy  
(Gao et al., 2019; Hannadige et al., 2021). NN methods can be also used to predict the polarimetric reflectance associated with  
complex water optical properties (Mukherjee et al., 2020), instantaneous photosynthetically available radiation models within  
450 ocean bodies (Aryal et al., 2022), and derive in-water optical properties from top of atmosphere MAP measurements for PACE  
(Agaglia et al., 2023).

Based ~~Therefore, based~~ on the improved NN forward models, this study provided an efficient space-borne MAP data processing  
algorithm, and discussed the data product and their associated uncertainties analyzed from a global scale synthetic HARP2  
dataset. For the future application to the real satellite data after PACE launch, it would be important to ensure the forward  
455 model is appropriate for the measurements by conducting input data quality control and data screening (Gao et al., 2021b).  
Further evaluations on the measurement uncertainty model can be conducted by comparing with fitting residual statistics  
(Gao et al., 2023). The algorithm and uncertainty analysis provide a viable way to process global HARP2 data, and improve  
our capability to observe, understand, and protect our environment.

## Appendix A: Evaluation of NN forward model uncertainty

460 As discussed in ~~See~~ Sect. 2, to evaluate the NN uncertainty interpedently, we use an additional 1000 set of simulation to with  
realistic HARP geometries formulated by Gao et al. (2021b). To further evaluate the accuracy of the NN, both mean average

error (MAE) and root mean square error (RMSE) are computed for both reflectance and DoLP as shown in Fig. A1 and Table A1. As discussed in Gao et al. (2022), MAE is more robust than RMSE to outliers. We estimate the NN uncertainties using MAE as  $\sigma_{NN} = \pi/2 \times MAE$ , which is equivalent by assuming the error following a Gaussian distribution (Gao et al., 2022). 465 Note that the RMSE is slightly larger than  $\sigma_{NN}$ . The estimated errors are similar to the results obtained in Gao et al. (2021a), where 20k training data each sampled with 100 angles are used. Here, we decreased the training data set to 10k, but sampled each case at 1000 angles. Note that in this study, we have included the angles with sunglint, which includes many more cases in the uncertainty evaluations. To further improve the accuracy, we need increase both the NN size and training data volume. a 470 balance of training data volume, NN speed (smaller size), NN accuracy (larger size, larger training data volume) are discussed in [See Sect. 2](#). NN accuracy are estimated with a value of 0.5% for NN size of  $512^3$ , and a value of 0.002 for [DoLP](#) using  $512^3$ , both are slightly larger than estimation from the training cost function but in a similar scale as discussed in [See Sect. 2](#). The estimated NN uncertainties can be included in the total uncertainty model in the retrieval cost function as discussed by Gao et al. (2021a).

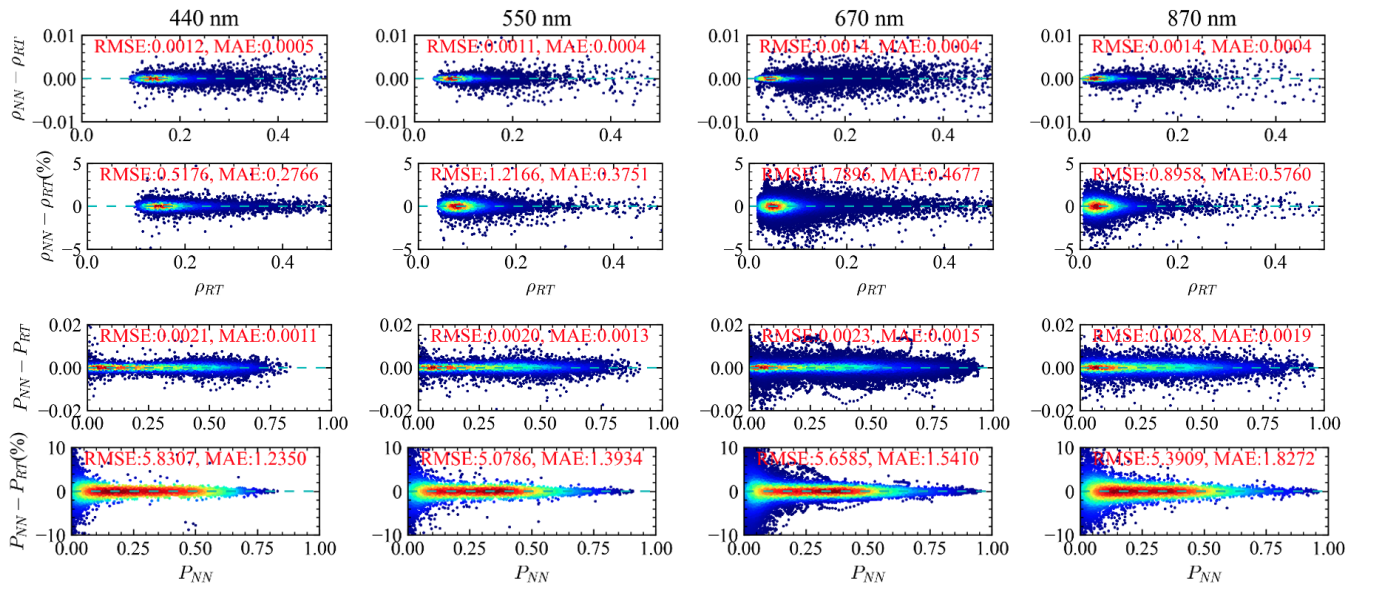


**Figure A1.** Comparison between the radiative transfer simulation and NN prediction, left panel: reflectance ( $\rho$ ); right panel: DoLP ( $P$ ). The scatter plots are shown in the top panel, the absolute different in the middle panel, and the percentage difference in the bottom panel. For each plot, the data points for the 550, 660 and 870nm bands are shifted upward by constant offsets consecutively as indicated by the solid cyan lines.

**Table A1.** Comparisons of the uncertainties for reflectance ( $\rho$ ) and DoLP (P) for both measurement and forward model including calibration uncertainty ( $\sigma_{cal}$ ), the radiative transfer simulation uncertainty ( $\sigma_{RT}$ ), and the NN uncertainty ( $\sigma_{NN}$ ). The percentage values listed in the table indicate the percentage uncertainties.)

Quantities	Uncertainties	440nm	550nm	670nm	870nm
$\rho_t$	$\sigma_{cal}$	3%	3%	3%	3%
	$\sigma_{RT}$	0.00012 (0.08%)	0.00005 (0.07%)	0.00010 (0.2%)	0.00015 (0.4%)
	RMSE <sub>NN</sub>	0.0012(0.52%)	0.0011(1.22%)	0.0014(1.79%)	0.0014(0.90%)
	MAE <sub>NN</sub>	0.0005(0.28%)	0.0004(0.38%)	0.0004(0.47%)	0.0004(0.58%)
	$\sigma_{NN}$	0.0007(0.35%)	0.0005(0.47%)	0.0005(0.59%)	0.0005(0.72%)
$P_t$	$\sigma_{cal}$	0.005	0.005	0.005	0.005
	$\sigma_{RT}$	0.0002	0.0002	0.0005	0.0007
	RMSE <sub>NN</sub>	0.0021	0.0020	0.0023	0.0028
	MAE <sub>NN</sub>	0.0011	0.0013	0.0015	0.0019
	$\sigma_{NN}$	0.0014	0.0016	0.0018	0.0023

*Acknowledgements.* The authors would like to thank Joel Gales, Wayne Roberson, Sean Foley for supports and discussions, and thank the

475 Ocean Biology Processing Group (OBPG) system team for support in High Performance Computing (HPC).

Meng Gao, Bryan A. Franz, Kirk Knobelspiesse, Brian Cairns, Amir Ibrahim, Frederick Patt, Andrew M. Sayer, and P. Jeremy Werdell have been supported by the NASA PACE project. P. Zhai recognizes the support from the PACE Science and Application Team ( NASA grants 80NSSC20M0227).

*Competing interests.* At least one of the (co-)authors is a member of the editorial board of Atmospheric Measurement Techniques. The

480 peer-review process was guided by an independent editor, and the authors also have no other competing interests to declare.

*Data availability.* Relevant data from this study can be accessed below.

PACE L1C grids: <https://oceandata.sci.gsfc.nasa.gov/directdataaccess/Level-1C/PACE-spacecraft/2022/080/>

Ancillary data: <https://oceandata.sci.gsfc.nasa.gov/directdataaccess/Ancillary/PACE-spacecraft/2022/>

L1C data: <https://oceandata.sci.gsfc.nasa.gov/directdataaccess/Level-1C/PACE-HARP2/2022/080/>

485 *Author contributions.* MG, BAF, KK formulated the study concept. MG generated the scientific data and wrote the original manuscript. PWZ developed the radiative transfer model with supports from NH. XX, AP and JVM provided and advised on the HARP data. FP, BF and

JW advised on the algorithm testing process. PC provided and advised on MERRA2 data and tables. AS, AI, GF, OH, YH and BC advised on the inversion and uncertainty methodologies. All authors provided critical feedback and edited the manuscript.

## References

490 The 2022 GCOS ECVs Requirements (GCOS 245), World Meteorological Organization, 2022.

Agaglato, J., Foster, R., Ibrahim, A., and Gilerson, A.: A neural network approach to the estimation of in-water attenuation to absorption ratios from PACE mission measurements, *Frontiers in Remote Sensing*, 4, <https://doi.org/10.3389/frsen.2023.1060908>, 2023.

Aggarwal, C. C.: *Neural Networks and Deep Learning: A Textbook*, Springer, Cham, Switzerland, 2018.

Anderson, G., Clough, S., Kneizys, F., Chetwynd, J., and Shettle, E.: AFGL Atmospheric Constituent Profiles (0.120km), AFGL-TR-86-495 0110, Air Force Geophysics Lab., Hanscom AFB, MA (USA), 1986.

Aryal, K., Zhai, P.-W., Gao, M., and Franz, B. A.: Instantaneous photosynthetically available radiation models for ocean waters using neural networks, *Appl. Opt.*, 61, 9985–9995, <https://doi.org/10.1364/AO.474914>, 2022.

Baydin, A. G., Pearlmutter, B. A., Radul, A. A., and Siskind, J. M.: Automatic differentiation in machine learning: a survey, *Journal of Machine Learning Research*, 18, 1–43, 2018.

500 Branch, M. A., Coleman, T. F., and Li, Y.: A Subspace, Interior, and Conjugate Gradient Method for Large-Scale Bound-Constrained Minimization Problems, *SIAM Journal on Scientific Computing*, 21, 1–23, <https://doi.org/10.1137/S1064827595289108>, 1999.

Buchard, V., Randles, C. A., da Silva, A. M., Darmenov, A., Colarco, P. R., Govindaraju, R., Ferrare, R., Hair, J., Beyersdorf, A. J., Ziembka, L. D., and Yu, H.: The MERRA-2 Aerosol Reanalysis, 1980 Onward. Part II: Evaluation and Case Studies, *Journal of Climate*, 30, 6851 – 6872, <https://doi.org/https://doi.org/10.1175/JCLI-D-16-0613.1>, 2017.

505 Cairns, B., E. Russell, E., and D. Travis, L.: Research Scanning Polarimeter: calibration and ground-based measurements, *Proc. SPIE*, 3754, 186–196, <https://doi.org/10.1117/12.366329>, 1999.

Castellanos, P., Da Silva, A. M., Darmenov, A. S., Buchard, V., Govindaraju, R. C., Ciren, P., and Kondragunta, S.: A Geostationary Instrument Simulator for Aerosol Observing System Simulation Experiments, *Atmosphere*, 10, <https://doi.org/10.3390/atmos10010002>, 2019.

510 Chen, C., Dubovik, O., Fuertes, D., Litvinov, P., Lapyonok, T., Lopatin, A., Ducos, F., Derimian, Y., Herman, M., Tanré, D., Remer, L. A., Lyapustin, A., Sayer, A. M., Levy, R. C., Hsu, N. C., Descloitres, J., Li, L., Torres, B., Karol, Y., Herrera, M., Herreras, M., Aspetsberger, M., Wanzenboeck, M., Bindreiter, L., Marth, D., Hangler, A., and Federspiel, C.: Validation of GRASP algorithm product from POLDER-/PARASOL data and assessment of multi-angular polarimetry potential for aerosol monitoring, *Earth System Science Data Discussions*, 12, 3573–3620, <https://doi.org/10.5194/essd-2020-224>, 2020.

515 Chen, C., Dubovik, O., Schuster, G. L., Chin, M., Henze, D. K., Lapyonok, T., Li, Z., Derimian, Y., and Zhang, Y.: Multi-angular polarimetric remote sensing to pinpoint global aerosol absorption and direct radiative forcing, *Nature Communications*, 13, 7459, <https://doi.org/10.1038/s41467-022-35147-y>, 2022.

Chen, N., Li, W., Gatebe, C., Tanikawa, T., Hori, M., Shimada, R., Aoki, T., and Stamnes, K.: New neural network cloud mask algorithm based on radiative transfer simulations, *Remote Sensing of Environment*, 219, 62–71, <https://doi.org/https://doi.org/10.1016/j.rse.2018.09.029>, 2018.

520 Chowdhary, J., Cairns, B., Mishchenko, M. I., Hobbs, P. V., Cota, G. F., Redemann, J., Rutledge, K., Holben, B. N., and Russell, E.: Retrieval of Aerosol Scattering and Absorption Properties from Photopolarimetric Observations over the Ocean during the CLAMS Experiment, *Journal of the Atmospheric Sciences*, 62, 1093–1117, <https://doi.org/10.1175/JAS3389.1>, 2005.

Cox, C. and Munk, W.: Measurement of the Roughness of the Sea Surface from Photographs of the Sun's Glitter, *J. Opt. Soc. Am.*, 44, 838–850, 1954.

525 Di Noia, A., Hasekamp, O. P., van Harten, G., Rietjens, J. H. H., Smit, J. M., Snik, F., Henzing, J. S., de Boer, J., Keller, C. U., and Volten, H.: Use of neural networks in ground-based aerosol retrievals from multi-angle spectropolarimetric observations, *Atmospheric Measurement Techniques*, 8, 281–299, <https://doi.org/10.5194/amt-8-281-2015>, 2015.

530 Diego, G. and Loyola, R.: Using neural network ensembles for the operational retrieval of ozone total columns, in: *IGARSS 2004. 2004 IEEE International Geoscience and Remote Sensing Symposium*, vol. 2, pp. 1041–1044 vol.2, <https://doi.org/10.1109/IGARSS.2004.1368589>, 2004.

Diner, D. J., Boland, S. W., Brauer, M., Bruegge, C., Burke, K. A., Chipman, R., Girolamo, L. D., Garay, M. J., Hasheminassab, S., Hyer, E., Jerrett, M., Jovanovic, V., Kalashnikova, O. V., Liu, Y., Lyapustin, A. I., Martin, R. V., Nastan, A., Ostro, B. D., Ritz, B., Schwartz, J., Wang, J., and Xu, F.: Advances in multiangle satellite remote sensing of speciated airborne particulate matter and association with adverse health effects: from MISR to MAIA, *Journal of Applied Remote Sensing*, 12, 1 – 22, <https://doi.org/10.1117/1.JRS.12.042603>, 2018.

535 Duan, M., Min, Q., and Li, J.: A fast radiative transfer model for simulating high-resolution absorption bands, *Journal of Geophysical Research: Atmospheres*, 110, <https://doi.org/https://doi.org/10.1029/2004JD005590>, 2005.

Dubovik, O., Sinyuk, A., Lapyonok, T., Holben, B. N., Mishchenko, M., Yang, P., Eck, T. F., Volten, H., Muñoz, O., Veihelmann, B., van der Zande, W. J., Leon, J.-F., Sorokin, M., and Slutsker, I.: Application of spheroid models to account for aerosol particle nonsphericity in remote sensing of desert dust, *Journal of Geophysical Research: Atmospheres*, 111, D11 208, <https://doi.org/10.1029/2005JD006619>, 2006.

540 Dubovik, O., Herman, M., Holdak, A., Lapyonok, T., Tanré, D., Deuzé, J. L., Ducos, F., Sinyuk, A., and Lopatin, A.: Statistically optimized inversion algorithm for enhanced retrieval of aerosol properties from spectral multi-angle polarimetric satellite observations, *Atmospheric Measurement Techniques*, 4, 975–1018, <https://doi.org/10.5194/amt-4-975-2011>, 2011.

Dubovik, O., Lapyonok, T., Litvinov, P., Herman, M., Fuertes, D., Ducos, F., Lopatin, A., Chaikovsky, A., Torres, B., Derimian, Y., 545 Huang, X., Aspetsberger, M., and Federspiel, C.: GRASP: a versatile algorithm for characterizing the atmosphere, SPIE Newsroom, <https://doi.org/10.1117/2.1201408.005558>, 2014.

Dubovik, O., Li, Z., Mishchenko, M. I., Tanré, D., Karol, Y., Bojkov, B., Cairns, B., Diner, D. J., Espinosa, W. R., Goloub, P., Gu, X., Hasekamp, O., Hong, J., Hou, W., Knobelgesse, K. D., Landgraf, J., Li, L., Litvinov, P., Liu, Y., Lopatin, A., Marbach, T., Marling, H., Martins, V., Meijer, Y., Milinevsky, G., Mukai, S., Parol, F., Qiao, Y., Remer, L., Rietjens, J., Sano, I., Stammes, P., Stammes, S., Sun, X., Tabary, P., Travis, L. D., Waquet, F., Xu, F., Yan, C., and Yin, D.: Polarimetric remote sensing of atmospheric aerosols: Instruments, methodologies, results, and perspectives, *Journal of Quantitative Spectroscopy and Radiative Transfer*, 224, 474 – 511, <https://doi.org/https://doi.org/10.1016/j.jqsrt.2018.11.024>, 2019.

550 Fan, C., Fu, G., Di Noia, A., Smit, M., Rietjens, J. H., A. Ferrare, R., Burton, S., Li, Z., and P. Hasekamp, O.: Use of A Neural Network-Based Ocean Body Radiative Transfer Model for Aerosol Retrievals from Multi-Angle Polarimetric Measurements, *Remote Sensing*, 11, 2877, <https://doi.org/10.3390/rs11232877>, 2019.

Fan, Y., Li, W., Gatebe, C. K., Jamet, C., Zibordi, G., Schroeder, T., and Stammes, K.: Atmospheric correction over coastal waters using multilayer neural networks, *Remote Sensing of Environment*, 199, 218–240, <http://www.sciencedirect.com/science/article/pii/S0034425717303310>, 2017.

Fougne, B., Marbach, T., Lacan, A., Lang, R., Schlüssel, P., Poli, G., Munro, R., and Couto, A. B.: The multi-viewing multi-channel 560 multi-polarisation imager – Overview of the 3MI polarimetric mission for aerosol and cloud characterization, *Journal of Quantitative Spectroscopy and Radiative Transfer*, 219, 23 – 32, <https://doi.org/https://doi.org/10.1016/j.jqsrt.2018.07.008>, 2018.

565 Frouin, R. J., Franz, B. A., Ibrahim, A., Knobelispiesse, K., Ahmad, Z., Cairns, B., Chowdhary, J., Dierssen, H. M., Tan, J., Dubovik, O.,  
Huang, X., Davis, A. B., Kalashnikova, O., Thompson, D. R., Remer, L. A., Boss, E., Coddington, O., Deschamps, P.-Y., Gao, B.-C.,  
Gross, L., Hasekamp, O., Omar, A., Pelletier, B., Ramon, D., Steinmetz, F., and Zhai, P.-W.: Atmospheric Correction of Satellite Ocean-  
Color Imagery During the PACE Era, *Frontiers in Earth Science*, 7, 145, <https://doi.org/10.3389/feart.2019.00145>, 2019.

570 Fu, G. and Hasekamp, O.: Retrieval of aerosol microphysical and optical properties over land using a multimode approach, *Atmospheric Measurement Techniques*, 11, 6627–6650, <https://doi.org/10.5194/amt-11-6627-2018>, 2018.

575 Fu, G., Hasekamp, O., Rietjens, J., Smit, M., Di Noia, A., Cairns, B., Wasilewski, A., Diner, D., Xu, F., Knobelispiesse, K.,  
Gao, M., da Silva, A., Burton, S., Hostetler, C., Hair, J., and Ferrare, R.: Aerosol retrievals from different polarimeters during  
580 the ACEPOLcampaign using a common retrieval algorithm, *Atmospheric Measurement Techniques Discussions*, 13, 553–573,  
<https://doi.org/https://doi.org/10.5194/amt-13-553-2020>, 2020.

Gao, M., Zhai, P.-W., Franz, B., Hu, Y., Knobelispiesse, K., Werdell, P. J., Ibrahim, A., Xu, F., and Cairns, B.: Retrieval of aerosol properties and water-leaving reflectance from multi-angular polarimetric measurements over coastal waters, *Opt. Express*, 26, 8968–8989,  
<https://doi.org/10.1364/OE.26.008968>, 2018.

585 Gao, M., Zhai, P.-W., Franz, B. A., Hu, Y., Knobelispiesse, K., Werdell, P. J., Ibrahim, A., Cairns, B., and Chase, A.: Inversion of multi-angular polarimetric measurements over open and coastal ocean waters: a joint retrieval algorithm for aerosol and water-leaving radiance properties, *Atmospheric Measurement Techniques*, 12, 3921–3941, <https://doi.org/10.5194/amt-12-3921-2019>, 2019.

590 Gao, M., Franz, B. A., Knobelispiesse, K., Zhai, P.-W., Martins, V., Burton, S., Cairns, B., Ferrare, R., Gales, J., Hasekamp, O.,  
Hu, Y., Ibrahim, A., McBride, B., Puthukkudy, A., Werdell, P. J., and Xu, X.: Efficient multi-angle polarimetric inversion of aerosols and ocean color powered by a deep neural network forward model, *Atmospheric Measurement Techniques*, 14, 4083–4110,  
<https://doi.org/10.5194/amt-14-4083-2021>, 2021a.

Gao, M., Knobelispiesse, K., Franz, B. A., Zhai, P.-W., Martins, V., Burton, S. P., Cairns, B., Ferrare, R., Fenn, M. A., Hasekamp, O., Hu,  
Y., Ibrahim, A., Sayer, A. M., Werdell, P. J., and Xu, X.: Adaptive Data Screening for Multi-Angle Polarimetric Aerosol and Ocean Color  
595 Remote Sensing Accelerated by Deep Learning, *Frontiers in Remote Sensing*, 2, 46, <https://doi.org/10.3389/frsen.2021.757832>, 2021b.

585 Gao, M., Knobelispiesse, K., Franz, B. A., Zhai, P.-W., Sayer, A. M., Ibrahim, A., Cairns, B., Hasekamp, O., Hu, Y., Martins, V., Werdell,  
P. J., and Xu, X.: Effective uncertainty quantification for multi-angle polarimetric aerosol remote sensing over ocean, *Atmospheric Measurement Techniques*, 15, 4859–4879, <https://doi.org/10.5194/amt-15-4859-2022>, 2022.

Gao, M., Knobelispiesse, K., Franz, B. A., Zhai, P.-W., Cairns, B., Xu, X., and Martins, J. V.: The impact and estimation of uncertainty  
590 correlation for multi-angle polarimetric remote sensing of aerosols and ocean color, *Atmospheric Measurement Techniques*, 16, 2067–  
2087, <https://doi.org/10.5194/amt-16-2067-2023>, 2023.

Gassó, S. and Knobelispiesse, K. D.: Circular polarization in atmospheric aerosols, *Atmospheric Chemistry and Physics*, 22, 13 581–13 605,  
<https://doi.org/10.5194/acp-22-13581-2022>, 2022.

595 Gelaro, R., McCarty, W., Suárez, M. J., Todling, R., Molod, A., Takacs, L., Randles, C. A., Darmenov, A., Bosilovich, M. G., Reichle,  
R., Wargan, K., Coy, L., Cullather, R., Draper, C., Akella, S., Buchard, V., Conaty, A., da Silva, A. M., Gu, W., Kim, G.-K., Koster, R.,  
Lucchesi, R., Merkova, D., Nielsen, J. E., Partyka, G., Pawson, S., Putman, W., Rienecker, M., Schubert, S. D., Sienkiewicz, M., and Zhao,  
B.: The Modern-Era Retrospective Analysis for Research and Applications, Version 2 (MERRA-2), *Journal of Climate*, 30, 5419–5454,  
<https://doi.org/10.1175/JCLI-D-16-0758.1>, 2017.

Hannadige, N. K., Zhai, P.-W., Gao, M., Franz, B. A., Hu, Y., Knobelispiesse, K., Werdell, P. J., Ibrahim, A., Cairns, B., and Hasekamp, O. P.: Atmospheric correction over the ocean for hyperspectral radiometers using multi-angle polarimetric retrievals, *Opt. Express*, 29, 4504–4522, <https://doi.org/10.1364/OE.408467>, 2021.

600 Hannadige, N. K., Zhai, P.-W., Gao, M., Hu, Y., Werdell, P. J., Knobelispiesse, K., and Cairns, B.: Performance evaluation of three bio-optical models in aerosol and ocean color joint retrievals, *Atmospheric Measurement Techniques Discussions*, 2023, 1–31, <https://doi.org/10.5194/amt-2023-142>, 2023.

Hasekamp, O. P. and Landgraf, J.: Linearization of vector radiative transfer with respect to aerosol properties and its use in satellite remote sensing, *Journal of Geophysical Research: Atmospheres*, 110, D04 203, [https://doi.org/https://doi.org/10.1029/2004JD005260](https://doi.org/10.1029/2004JD005260), 2005.

605 Hasekamp, O. P. and Landgraf, J.: Retrieval of aerosol properties over land surfaces: capabilities of multiple-viewing-angle intensity and polarization measurements, *Appl. Opt.*, 46, 3332–3344, <https://doi.org/10.1364/AO.46.003332>, 2007.

Hasekamp, O. P., Litvinov, P., and Butz, A.: Aerosol properties over the ocean from PARASOL multiangle photopolarimetric measurements, *Journal of Geophysical Research: Oceans*, 116, D14 204, [https://doi.org/https://doi.org/10.1029/2010JD015469](https://doi.org/10.1029/2010JD015469), 2011.

610 Hasekamp, O. P., Fu, G., Rusli, S. P., Wu, L., Noia, A. D., aan de Brugh, J., Landgraf, J., Smit, J. M., Rietjens, J., and van Amerongen, A.: Aerosol measurements by SPEXone on the NASA PACE mission: expected retrieval capabilities, *Journal of Quantitative Spectroscopy and Radiative Transfer*, 227, 170 – 184, [https://doi.org/https://doi.org/10.1016/j.jqsrt.2019.02.006](https://doi.org/10.1016/j.jqsrt.2019.02.006), 2019a.

Hasekamp, O. P., Gryspeerd, E., and Quaas, J.: Analysis of polarimetric satellite measurements suggests stronger cooling due to aerosol–cloud interactions, *Nature Communications*, 10, 5405, <https://doi.org/10.1038/s41467-019-13372-2>, 2019b.

615 Hioki, S., Riedi, J., and Djellali, M. S.: A study of polarimetric error induced by satellite motion: application to the 3MI and similar sensors, *Atmospheric Measurement Techniques*, 14, 1801–1816, <https://doi.org/10.5194/amt-14-1801-2021>, 2021.

Ibrahim, A., Franz, B. A., Sayer, A. M., Knobelispiesse, K., Zhang, M., Bailey, S. W., McKenna, L. I. W., Gao, M., and Werdell, P. J.: Optimal estimation framework for ocean color atmospheric correction and pixel-level uncertainty quantification, *Appl. Opt.*, 61, 6453–6475, <https://doi.org/10.1364/AO.461861>, 2022.

620 Jia, H., Quaas, J., Gryspeerd, E., Böhm, C., and Sourdeval, O.: Addressing the difficulties in quantifying droplet number response to aerosol from satellite observations, *Atmospheric Chemistry and Physics*, 22, 7353–7372, <https://doi.org/10.5194/acp-22-7353-2022>, 2022.

Kahn, R.: SATELLITES AND SATELLITE REMOTE SENSING | Aerosol Measurements, in: *Encyclopedia of Atmospheric Sciences* (Second Edition), edited by North, G. R., Pyle, J., and Zhang, F., pp. 51–66, Academic Press, Oxford, second edition edn., <https://doi.org/https://doi.org/10.1016/B978-0-12-382225-3.00347-9>, 2015.

625 Kaufman, Y. J., Tanré, D., and Boucher, O.: A satellite view of aerosols in the climate system, *Nature*, 419, 215–223, <https://doi.org/10.1038/nature01091>, 2002.

Kawata, Y.: Circular polarization of sunlight reflected by planetary atmospheres, *Icarus*, 33, 217 – 232, [https://doi.org/https://doi.org/10.1016/0019-1035\(78\)90035-0](https://doi.org/https://doi.org/10.1016/0019-1035(78)90035-0), 1978.

Knobelispiesse, K., Cairns, B., Mishchenko, M., Chowdhary, J., Tsigaridis, K., van Diedenhoven, B., Martin, W., Ottaviani, M., and Alexander, M.: Analysis of fine-mode aerosol retrieval capabilities by different passive remote sensing instrument designs, *Optics Express*, 20, 21 457–21 484, <https://doi.org/10.1364/OE.20.021457>, 2012.

Koepke, P.: *Remote Sensing Signatures of Whitecaps*, 1984.

630 Kokhanovsky, A., Davis, A., Cairns, B., Dubovik, O., Hasekamp, O., Sano, I., Mukai, S., Rozanov, V., Litvinov, P., Lapyonok, T., Kolomiets, I., Oberemok, Y., Savenkov, S., Martin, W., Wasilewski, A., Di Noia, A., Stap, F., Rietjens, J., Xu, F., Natraj, V., Duan, M., Cheng, T., and

635 Munro, R.: Space-based remote sensing of atmospheric aerosols: The multi-angle spectro-polarimetric frontier, *Earth-Science Reviews*, 145, 85–116, [https://doi.org/https://doi.org/10.1016/j.earscirev.2015.01.012](https://doi.org/10.1016/j.earscirev.2015.01.012), 2015.

Kokhanovsky, A. A.: Parameterization of the Mueller matrix of oceanic waters, *Journal of Geophysical Research: Oceans*, 108, 3175, 2003.

Lacagnina, C., Hasekamp, O. P., and Torres, O.: Direct radiative effect of aerosols based on PARASOL and OMI satellite observations, *Journal of Geophysical Research: Atmospheres*, 122, 2366–2388, [https://doi.org/https://doi.org/10.1002/2016JD025706](https://doi.org/10.1002/2016JD025706), 2017.

640 Lang, R., Poli, G., Fougnie, B., Lacan, A., Marbach, T., Riedi, J., Schlüssel, P., Couto, A. B., and Munro, R.: The 3MI Level-1C geo-projected product – definition and processing description, *Journal of Quantitative Spectroscopy and Radiative Transfer*, 225, 91–109, [https://doi.org/https://doi.org/10.1016/j.jqsrt.2018.12.022](https://doi.org/10.1016/j.jqsrt.2018.12.022), 2019.

Li, L., Dubovik, O., Derimian, Y., Schuster, G. L., Lapyonok, T., Litvinov, P., Ducos, F., Fuertes, D., Chen, C., Li, Z., Lopatin, A., Torres, B., and Che, H.: Retrieval of aerosol components directly from satellite and ground-based measurements, *Atmospheric Chemistry and Physics*, 19, 13 409–13 443, <https://doi.org/10.5194/acp-19-13409-2019>, 2019.

645 Li, Z., Hou, W., Hong, J., Zheng, F., Luo, D., Wang, J., Gu, X., and Qiao, Y.: Directional Polarimetric Camera (DPC): Monitoring aerosol spectral optical properties over land from satellite observation, *Journal of Quantitative Spectroscopy and Radiative Transfer*, 218, 21 – 37, [https://doi.org/https://doi.org/10.1016/j.jqsrt.2018.07.003](https://doi.org/10.1016/j.jqsrt.2018.07.003), 2018.

Martins, J. V., Fernandez-Borda, R., McBride, B., Remer, L., and Barbosa, H. M. J.: The HARP hyperangular imaging polarimeter and the need for small satellite payloads with high science payoff for earth science remote sensing, in: IGARSS 2018 - 2018 IEEE International Geoscience and Remote Sensing Symposium, Valencia, Spain, July 22-27, 2018, pp. 6304–6307, <https://doi.org/10.1109/IGARSS.2018.8518823>, 2018.

650 McBride, B. A., Martins, J. V., Cieslak, J. D., Fernandez-Borda, R., Puthukuddy, A., Xu, X., Sienkiewicz, N., Cairns, B., and Barbosa, H. M. J.: Pre-launch calibration and validation of the Airborne Hyper-Angular Rainbow Polarimeter (AirHARP) instrument, *EGUspHERE*, 2023, 1–52, <https://doi.org/10.5194/egusphere-2023-865>, 2023.

Meister, G., Knuble, J. J., Chemerys, L. H., Choi, H., Collins, N. R., Eplee, R. E., Gliese, U., Gorman, E. T., Jepsen, K., Kitchen-McKinley, S., Lee, S., McIntire, J. W., Patt, F. S., Tse, B. C., Waluschka, E., and Werdell, P. J.: Test Results From the Prelaunch Characterization Campaign of the Engineering Test Unit of the Ocean Color Instrument of NASA's Plankton, Aerosol, Cloud and Ocean Ecosystem (PACE) Mission, *Frontiers in Remote Sensing*, 3, <https://doi.org/10.3389/frsen.2022.875863>, 2022.

660 Mishchenko, M. I. and Travis, L. D.: Satellite retrieval of aerosol properties over the ocean using polarization as well as intensity of reflected sunlight, *Journal of Geophysical Research: Atmospheres*, 102, 16 989–17 013, <https://doi.org/10.1029/96JD02425>, 1997.

Mishchenko, M. I., Travis, L. D., and Lacis, A. A.: *Scattering, Absorption, and Emission of Light by Small Particles*, Cambridge University Press, Cambridge, England, 2002.

665 Mishchenko, M. I., Cairns, B., Hansen, J. E., Travis, L. D., Burg, R., Kaufman, Y. J., Vanderlei Martins, J., and Shettle, E. P.: Monitoring of aerosol forcing of climate from space: analysis of measurement requirements, *Journal of Quantitative Spectroscopy and Radiative Transfer*, 88, 149–161, [https://doi.org/https://doi.org/10.1016/j.jqsrt.2004.03.030](https://doi.org/10.1016/j.jqsrt.2004.03.030), photopolarimetry in remote sensing, 2004.

Mukherjee, L., Zhai, P.-W., Gao, M., Hu, Y., A. Franz, B., and Werdell, P. J.: Neural Network Reflectance Prediction Model for Both Open Ocean and Coastal Waters, *Remote Sensing*, 12, 1421, <https://doi.org/10.3390/rs12091421>, 2020.

Nanda, S., de Graaf, M., Veefkind, J. P., ter Linden, M., Sneep, M., de Haan, J., and Levelt, P. F.: A neural network radiative transfer model approach applied to the Tropospheric Monitoring Instrument aerosol height algorithm, *Atmospheric Measurement Techniques*, 12, 6619–6634, <https://doi.org/10.5194/amt-12-6619-2019>, 2019.

Osawa, K., Tsuji, Y., Ueno, Y., Naruse, A., Yokota, R., and Matsuoka, S.: Large-Scale Distributed Second-Order Optimization Using Kronecker-Factored Approximate Curvature for Deep Convolutional Neural Networks, Proceedings of the IEEE/CVF Conference on Computer Vision and Pattern Recognition (CVPR), 2019.

675 Plankton, Aerosol, Cloud, ocean Ecosystem (PACE) mission: The PACE Level 1C data format, [https://oceancolor.gsfc.nasa.gov/data/pace/PACE\\_L1C\\_Format\\_DRAFTv20200918.pdf](https://oceancolor.gsfc.nasa.gov/data/pace/PACE_L1C_Format_DRAFTv20200918.pdf), 2020.

Puthukkudy, A., Martins, J. V., Remer, L. A., Xu, X., Dubovik, O., Litvinov, P., McBride, B., Burton, S., and Barbosa, H. M. J.: Retrieval of aerosol properties from Airborne Hyper-Angular Rainbow Polarimeter (AirHARP) observations during ACEPOL 2017, Atmospheric Measurement Techniques, 13, 5207–5236, <https://doi.org/10.5194/amt-13-5207-2020>, 2020.

680 Pörtner, H.-O., Roberts, D., Tignor, M., Poloczanska, E., Mintenbeck, K., A. Alegría, M. C., Langsdorf, S., S. Löschke, Möller, V., Okem, A., and Rama, B., eds.: IPCC, 2022: Climate Change 2022: Impacts, Adaptation, and Vulnerability. Contribution of Working Group II to the Sixth Assessment Report of the Intergovernmental Panel on Climate Change, Cambridge University Press., In Press.

Randles, C. A., da Silva, A. M., Buchard, V., Colarco, P. R., Darmenov, A., Govindaraju, R., Smirnov, A., Holben, B., Ferrare, R., Hair, J., Shinozuka, Y., and Flynn, C. J.: The MERRA-2 Aerosol Reanalysis, 1980 Onward. Part I: System Description and Data Assimilation 685 Evaluation, Journal of Climate, 30, 6823 – 6850, <https://doi.org/10.1175/JCLI-D-16-0609.1>, 2017.

Remer, L. A., Davis, A. B., Mattoo, S., Levy, R. C., Kalashnikova, O. V., Coddington, O., Chowdhary, J., Knobelspiesse, K., Xu, X., Ahmad, Z., Boss, E., Cairns, B., Dierssen, H. M., Diner, D. J., Franz, B., Frouin, R., Gao, B.-C., Ibrahim, A., Martins, J. V., Omar, A. H., Torres, O., Xu, F., and Zhai, P.-W.: Retrieving Aerosol Characteristics From the PACE Mission, Part 1: Ocean Color Instrument, Frontiers in Earth Science, 7, 152, <https://doi.org/10.3389/feart.2019.00152>, 2019a.

690 Remer, L. A., Knobelspiesse, K., Zhai, P.-W., Xu, F., Kalashnikova, O. V., Chowdhary, J., Hasekamp, O., Dubovik, O., Wu, L., Ahmad, Z., Boss, E., Cairns, B., Coddington, O., Davis, A. B., Dierssen, H. M., Diner, D. J., Franz, B., Frouin, R., Gao, B.-C., Ibrahim, A., Levy, R. C., Martins, J. V., Omar, A. H., and Torres, O.: Retrieving Aerosol Characteristics From the PACE Mission, Part 2: Multi-Angle and Polarimetry, Frontiers in Environmental Science, 7, 94, <https://doi.org/10.3389/fenvs.2019.00094>, 2019b.

Rodgers, C.: Inverse Methods for Atmospheric Sounding: Theory and Practice, World Scientific World Scientific Publishing, Singapore, 695 <https://doi.org/10.1142/3171>, 2000.

Schroeder, T., Behnert, I., Schaale, M., Fischer, J., and Doerffer, R.: Atmospheric correction algorithm for MERIS above case-2 waters, International Journal of Remote Sensing, 28, 1469–1486, <https://doi.org/10.1080/01431160600962574>, 2007.

700 Shi, C., Hashimoto, M., Shiomi, K., and Nakajima, T.: Development of an Algorithm to Retrieve Aerosol Optical Properties Over Water Using an Artificial Neural Network Radiative Transfer Scheme: First Result From GOSAT-2/CAI-2, IEEE TRANSACTIONS ON GEOSCIENCE AND REMOTE SENSING, pp. 1–12, <https://doi.org/10.1109/TGRS.2020.3038892>, 2020.

Shorten, C. and Khoshgoftaar, T. M.: A survey on Image Data Augmentation for Deep Learning, Journal of Big Data, 6, 60, <https://doi.org/10.1186/s40537-019-0197-0>, 2019.

Silverman, B.: Density Estimation for Statistics and Data Analysis, Vol. 26, Monographs on Statistics and Applied Probability, London: Chapman and Hall, 1986., 1986.

705 Smit, J. M., Rietjens, J. H. H., van Harten, G., Noia, A. D., Laauwen, W., Rheingans, B. E., Diner, D. J., Cairns, B., Wasilewski, A., Knobelspiesse, K. D., Ferrare, R., and Hasekamp, O. P.: SPEX airborne spectropolarimeter calibration and performance, Appl. Opt., 58, 5695–5719, <https://doi.org/10.1364/AO.58.005695>, 2019.

Snyder, J. P.: Map projections—A working manual (Vol. 1395), US Government Printing Office., 1987.

Stamnes, S., Hostetler, C., Ferrare, R., Burton, S., Liu, X., Hair, J., Hu, Y., Wasilewski, A., Martin, W., van Diedenhoven, B., Chowdhary, J., Cetinić, I., Berg, L. K., Stamnes, K., and Cairns, B.: Simultaneous polarimeter retrievals of microphysical aerosol and ocean color parameters from the “MAPP” algorithm with comparison to high-spectral-resolution lidar aerosol and ocean products, *Appl. Opt.*, 57, 2394–2413, <https://doi.org/10.1364/AO.57.002394>, 2018.

710 Stamnes, S., Jones, M., Allen, J. G., Chemyakin, E., Bell, A., Chowdhary, J., Liu, X., Burton, S. P., Van Diedenhoven, B., Hasekamp, O., Hair, J., Hu, Y., Hostetler, C., Ferrare, R., Stamnes, K., and Cairns, B.: The PACE-MAPP algorithm: Simultaneous aerosol and ocean polarimeter products using coupled atmosphere-ocean vector radiative transfer, *Frontiers in Remote Sensing*, 4, <https://doi.org/10.3389/frsen.2023.1174672>, 2023.

715 Stegmann, P. G., Johnson, B., Moradi, I., Karpowicz, B., and McCarty, W.: A deep learning approach to fast radiative transfer, *Journal of Quantitative Spectroscopy and Radiative Transfer*, 280, 108 088, <https://doi.org/https://doi.org/10.1016/j.jqsrt.2022.108088>, 2022.

Tanré, D., Bréon, F. M., Deuzé, J. L., Dubovik, O., Ducos, F., François, P., Goloub, P., Herman, M., Lifermann, A., and Waquet, F.: Remote 720 sensing of aerosols by using polarized, directional and spectral measurements within the A-Train: the PARASOL mission, *Atmos. Meas. Tech.*, 4, 1383–1395, <https://doi.org/https://doi.org/10.5194/amt-4-1383-2011>, 2011.

Ukkonen, P.: Exploring Pathways to More Accurate Machine Learning Emulation of Atmospheric Radiative Transfer, *Journal of Advances in Modeling Earth Systems*, 14, e2021MS002875, <https://doi.org/https://doi.org/10.1029/2021MS002875>, e2021MS002875 2021MS002875, 2022.

725 Voss, K. J. and Fry, E. S.: Measurement of the Mueller matrix for ocean water, *Applied Optics*, 23, 4427–4439, 1984.

Wang, J. and Christopher, S. A.: Intercomparison between satellite-derived aerosol optical thickness and PM2.5 mass: Implications for air quality studies, *Geophysical Research Letters*, 30, <https://doi.org/https://doi.org/10.1029/2003GL018174>, 2003.

730 Wang, J., Xu, X., Ding, S., Zeng, J., Spurr, R., Liu, X., Chance, K., and Mishchenko, M.: A numerical testbed for remote sensing of aerosols, and its demonstration for evaluating retrieval synergy from a geostationary satellite constellation of GEO-CAPE and GOES-R, *Journal of Quantitative Spectroscopy and Radiative Transfer*, 146, 510 – 528, <https://doi.org/https://doi.org/10.1016/j.jqsrt.2014.03.020>, electromagnetic and Light Scattering by Nonspherical Particles XIV, 2014.

735 Waquet, F., Riedi, J., Labonne, L. C., Goloub, P., Cairns, B., Deuzé, J.-L., and Tanré, D.: Aerosol Remote Sensing over Clouds Using A-Train Observations, *Journal of the Atmospheric Sciences*, 66, 2468–2480, <https://doi.org/10.1175/2009jas3026.1>, 2009.

Wu, L., Hasekamp, O., van Diedenhoven, B., and Cairns, B.: Aerosol retrieval from multiangle, multispectral photopolarimetric 740 measurements: importance of spectral range and angular resolution, *Atmospheric Measurement Techniques*, 8, 2625–2638, <https://doi.org/10.5194/amt-8-2625-2015>, 2015.

Wu, L., Hasekamp, O., van Diedenhoven, B., Cairns, B., Yorks, J. E., and Chowdhary, J.: Passive remote sensing of aerosol layer height using near-UV multiangle polarization measurements, *Geophysical Research Letters*, 43, 8783–8790, <https://doi.org/https://doi.org/10.1002/2016GL069848>, 2016.

745 Xu, F., Dubovik, O., Zhai, P. W., Diner, D. J., Kalashnikova, O. V., Seidel, F. C., Litvinov, P., Bovchaliuk, A., Garay, M. J., van Harten, G., and Davis, A. B.: Joint retrieval of aerosol and water-leaving radiance from multispectral, multiangular and polarimetric measurements over ocean, *Atmospheric Measurement Techniques*, 9, 2877–2907, 2016.

Xu, F., van Harten, G., Diner, D. J., Kalashnikova, O. V., Seidel, F. C., Bruegge, C. J., and Dubovik, O.: Coupled retrieval of aerosol properties and land surface reflection using the Airborne Multiangle SpectroPolarimetric Imager, *Journal of Geophysical Research: Atmospheres*, 122, 7004–7026, <https://doi.org/10.1002/2017JD026776>, 2017.

Xu, F., Gao, L., Redemann, J., Flynn, C. J., Espinosa, W. R., da Silva, A. M., Stamnes, S., Burton, S. P., Liu, X., Ferrare, R., Cairns, B., and Dubovik, O.: A Combined Lidar-Polarimeter Inversion Approach for Aerosol Remote Sensing Over Ocean, *Frontiers in Remote Sensing*, 2, 2, <https://doi.org/10.3389/frsen.2021.620871>, 2021.

Zhai, P.-W. and Hu, Y.: An improved pseudo spherical shell algorithm for vector radiative transfer, *Journal of Quantitative Spectroscopy and Radiative Transfer*, 282, 108 132, <https://doi.org/https://doi.org/10.1016/j.jqsrt.2022.108132>, 2022.

Zhai, P.-W., Gao, M., Franz, B. A., Werdell, P. J., Ibrahim, A., Hu, Y., and Chowdhary, J.: A Radiative Transfer Simulator for PACE: Theory and Applications, *Frontiers in Remote Sensing*, 3, <https://doi.org/10.3389/frsen.2022.840188>, 2022.